Multiscale analysis of out-of-plane masonry elements using different structural models at macro and microscale

Daniela Addessi[a], Paolo Di Re[a], Cristina Gatta[a], Elio Sacco[b]*

[a]*Department of Structural and Geotechnical Engineering, Sapienza University of Rome,*
Via Eudossiana 18, 00184 Rome, Italy, {daniela.addessi, paolo.dire, cristina.gatta}@uniroma1.it
[b]*Department of Structures for Engineering and Architecture, University of Naples Federico II,*
Via Claudio 21, 80125 Naples, Italy, elio.sacco@unina.it

Abstract

A novel two-scale modeling approach, linking different structural models at macro and microscale, is proposed to describe response of masonry walls with periodic texture. At the higher macroscopic scale, the real heterogeneous material is modeled as a homogenized medium, considering the classical Mindlin-Reissner theory for flat shells. At the lower microscopic scale, a representative masonry Unit Cell (UC), accounting for the actual geometry, arrangement and nonlinear behavior of constituent materials, is analyzed in detail by resorting to a three-dimensional Cauchy model. The UC is modeled as the assembly of elastic bricks and nonlinear zero-thickness interfaces, in which the sliding frictional and damaging mechanisms are concentrated. To perform the macro-micro information transition a proper kinematic map is defined, whereas the up-scaling process is performed via a homogenization procedure based on the Transformation Field Analysis (TFA), properly extended to the case of interfaces. The developed homogenization procedure invokes a generalized Hill-Mandel principle and requires to satisfy 'non-standard' constraints at the microlevel, for which the perturbed Lagrangian method is employed.

Numerical applications are performed to prove the model efficiency in describing the response of a running bond UC subjected to in-plane and out-of-plane loads. Special attention is devoted to the analysis of shell bending and shear behavior, comparing the results obtained with the proposed model with those recovered by detailed micromechanical analyses.

Keywords: multiscale model, thick shell, masonry, damage-friction, 3D RVE, TFA approach.

1. Introduction

The structural assessment of masonry constructions is even now a challenging task due to their large spread in civil and architectural heritage of many countries. Commonly, these are ancient constructions built according to old technical codes or, in many cases, following good rules of thumb. Thus, their structural performance needs to be carefully assessed in order to evaluate and design repairing and strengthening interventions, if needed. The three main mechanisms, that can cause the collapse of masonry constructions, can be hierarchically classified as crumbling, out-of-plane and in-plane. Focusing on the out-of-plane masonry structural response, this plays a significant role on the construction stability. As a matter of fact, out-of-plane collapse of masonry walls is one of the main causes of human life loss and significant economic damage.

Many features influence the out-of-plane mechanism, such as texture of the brickwork, geometric and mechanical properties of the constituents, boundary conditions. In particular, the specific arrangement of

---

*Corresponding author: Elio Sacco (elio.sacco@unina.it)

the constituents, bricks/blocks and mortar, strongly determines the wall failure mechanism, ultimate strength and hysteretic dissipation associated to the collapse.

Several experimental tests were developed during the last two decades to investigate the influence of the actual texture on the masonry wall response, even in view of a possible reinforcement adopting FRP (Fiber Reinforced Polymers) or FRCM (Fiber Reinforced Cementitious Matrix). Many numerical procedures were also formulated relying on different approaches, ranging from the simplified tools to the most sophisticated models. A recent review of the modeling strategies for masonry construction can be found in [15].

An accurate, but computational very demanding, approach is the three-dimensional (3D) micromechanical modeling, which describes the detailed arrangement, geometry and mechanical response of the masonry constituents [4, 5, 27, 14]. This commonly adopts 3D solid finite elements for both bricks and mortar joints and introduces damage-plastic constitutive laws to account for the main occurring nonlinear mechanisms. Alternatively, zero-thickness cohesive-frictional interfaces are employed to model the mortar joints and their connections to the bricks [30]. Giambanco et al. in [19] formulated an interface element for mortar joints in masonry relying on elasto-plasticity for non-standard materials to simulate the softening response which occurs along with the decohesion process in presence of shear and tension tractions. Macorini and Izzudin in [21] proposed a 2D nonlinear interface element for modeling both mortar and brick-mortar interfaces in case of 3D arrangement for brick-masonry, accounting for the in-plane stacking mode and the through-thickness geometry. Lebon in [20] presented four interface models for masonry structures also referring to some experimental studies.

A fair compromise between modeling accuracy and computational efficiency is the multiscale approach, which constitutes one of the most modern and attractive method to study the response of structural elements made of heterogeneous materials. This analyzes the real construction at different scales, whose sizes depend on the problem tackled. Regarding masonry structures, two scales are usually considered corresponding to the structural (macroscale) and material (microscale) level. A fictitious homogenized continuum medium is adopted at the macroscale and, to derive the constitutive response at each macroscopic point, a downscaling is performed. Then, the response of a representative volume element (RVE), properly selected to describe the real material texture, is analyzed in detail [9, 22].

In the last decades, the so called computational homogenization methods have taken hold and a broad range of models was proposed for masonry in this framework. In these procedures micro and macroscale exchange information at each iteration of the global solution procedure [23, 16].

Usually, a parallel computing strategy is adopted to reduce the computational burden. A number of computational homogenization methods was proposed to study the nonlinear response of masonry structural elements subjected to in-plane loading, focusing on flexural and shear failure mechanisms. These can adopt the Cauchy continuum to model both macro and microscale, as well as higher-order, micropolar and Cosserat formulations mainly at the macroscale [16, 10]. Most of them use damage-plastic constitutive laws at the microscale to describe the nonlinear degrading and sliding friction mechanisms occurring in the masonry constituents, bricks and mortar, and adopt various techniques to regularize the numerical response in presence of strain-softening. Analogously to the micromechanical models, at the RVE level, continuum FEs or interface elements can be used to model the mortar joints. A first attempt to extend the homogenization procedure for periodic media, well consolidated for in-plane 2D masonry problems, to 3D strain and stress states was made by Anthoine [8], who underlined that the 2D formulation can be naturally extended to 3D masonry problems with three periodicity directions, that is in case of masonry bulks characterized by 3D periodic texture of bricks and mortar. Conversely, for masonry walls where only two directions of periodicity can be defined lying in the mid-plane, the trough-thickness direction needs a different and specific formulation. In this context, recently, some computational homogenization methods were formulated to describe masonry

failure mechanisms under out-of-plane loading. Addessi et al. [6, 2] proposed a two-scale model adopting beam formulations at both the macroscopic scale and the RVE level to study the out-of-plane response of masonry columns and walls characterized by cylindrical deformation mode. Mercatoris et al. [24, 25] proposed homogenized shell-like models to overcome the limits of the classical 3D homogenization. These approaches usually couple a 3D UC at the microscale to a shell model at the macro structural level. Most of the proposed models relies on the Kirchhoff-Love theory for thin shells, often assuming bricks as rigid and mortar modeled by interfaces [13], but some recent works discussing the homogenization procedure for thick shells based on the Mindlin theory can be found [12, 28].

Although very powerful and effective when employing parallel computing, multiscale procedures can result very cumbersome and time demanding. Thus, some simplified and interesting techniques were developed in the framework of the Reduced Order Models (ROM), aiming at significantly reducing the computational burden, although preserving the advantages of the multiscale modeling. Among the ROM techniques, the Transformation Field Analysis (TFA) [17, 26, 18] represents a very interesting and effective homogenization procedure, successfully adopted for different nonlinear composite materials. Several TFA versions for masonry were proposed in literature, mainly devoted to study the in-plane mechanical response of masonry panels [3].

This paper presents a multiscale model for the nonlinear in-plane and out-of-plane analysis of masonry walls. In particular, a regular masonry texture is considered, so that the masonry fabric can be assumed as repetitive and, hence, periodic. At the structural scale, a thick shell formulation is adopted, thus including both the membrane and thick plate strain and stress components at the macroscopic level. Because of the material periodicity in the wall mid-plane, at the microscale, a unit cell (UC) is selected and a full three-dimensional modeling is adopted, assuming zero traction on the two free opposite surfaces in the direction orthogonal to the thickness. A kinematic driven homogenization procedure is then performed, that is a kinematic map is defined on the basis of the introduced macroscopic strain measures. The displacement fields in the UC are represented as the additive composition of the assigned kinematic map and an unknown perturbation terms, satisfying periodicity conditions on the UC boundary, except for the free surfaces. Bricks response is modeled as linear elastic, while all the nonlinear damage and sliding friction mechanisms are concentrated in the mortar joints. These latter are modeled as zero-thickness interfaces, adopting and extending the formulation presented in [3] for the 2D UC to the 3D case. To obtain a fast and efficient multiscale procedure, a TFA-based technique is employed to solve the nonlinear homogenization problem, assuming that the nonlinear mechanisms are uniformly distributed in some subsets, properly defined in the UC according to the periodicity conditions and discretized through the thickness. Computational issues are discussed in detail, both concerning the micromechanical solution algorithm and the TFA procedure. Finally, some numerical examples are illustrated showing the response of the RVE under typical loading conditions simulating the in-plane and out-of-plane most relevant cases.

The paper is organized as follows. After the introduction, in Section 2 the multiscale procedure is discussed giving details on the governing equations at macro and microscale and the procedure for linking the two scales. Section 3 describes the TFA procedure developed to derive the reduced order model. Section 4 illustrates some specific computational aspects. Numerical applications are carried out in Section 5. Finally, concluding remarks are given in Section 6.

2. Multiscale procedure for masonry wall

A two-scale modeling approach is presented to describe in-plane and out-of-plane nonlinear mechanisms of masonry walls. Although a masonry wall is a heterogeneous 3D body, considering the common case in

which the wall thickness is significantly lower than the other two dimensions, the shell structural model is adopted at the macroscale, where an effective homogenized medium is considered. Moreover, to accurately account for the microscopic mechanisms arising between bricks and mortar, as discussed for instance in [1], a full 3D model is adopted at the microscale.

The two scales, macro and micro, are regarded as far enough to be considered as separated and a kinematic map is defined to link them. The separation of scale assumption is introduced here, considering the scale of the structural element much greater than the scale of the heterogeneities and, then, of the material. Indeed, the macro- and microscale are coupled as the overall constitutive response at the macroscale is derived by the analysis of the response at the microscale. To be noted is that in case of brittle or cohesive materials, an important information that have to be transferred from the micro- to the macroscale is the dissipated energy depending on the characteristic length (microstructural size) at the microscale. If correctly transferred, this information allows to avoid pathological mesh-dependency of the numerical response at the macroscale related to localization phenomena.

At both scales, small displacements and strains are assumed. A generalized Hill-Mandel principle is invoked to properly link the two scales and, thus, to evaluate the homogenized stress measures for the shell at the macroscale on the basis of the stresses computed for the constituents at the microscale.

2.1. Shell formulation at the macroscale

At the structural macroscopic scale, the real heterogeneous masonry wall characterized by periodic texture and constant thickness t is modeled as an equivalent homogenized shell, adopting the classical Mindlin-Reissner theory for flat shells. The Cartesian coordinate system (X_1, X_2, X_3) is introduced, with X_1 and X_2 lying in the shell mid-plane and X_3 running along the thickness. In the following, the in-plane quantities involved in the analysis are organized in vectors overlined with the hat symbol.

The 3D displacement fields $\mathbf{U} = \left\{ \hat{\mathbf{U}}^T \, U_3 \right\}^T$, with $\hat{\mathbf{U}} = \{U_1 \, U_2\}^T$ collecting the displacement components along directions X_1 and X_2 at each point $\mathbf{X} = \left\{ \hat{\mathbf{X}}^T \, X_3 \right\}^T$ of the wall and $\hat{\mathbf{X}} = \{X_1 \, X_2\}^T$, are represented according to the Mindlin shell theory in the form:

$$
\begin{aligned}
\hat{\mathbf{U}} \left(\hat{\mathbf{X}}, X_3 \right) &= \hat{\mathbf{V}} \left(\hat{\mathbf{X}} \right) + X_3 \, \mathbf{\Phi} \left(\hat{\mathbf{X}} \right) \\
U_3 \left(\hat{\mathbf{X}}, X_3 \right) &= V_3 \left(\hat{\mathbf{X}} \right)
\end{aligned}
\tag{1}
$$

where $\mathbf{V} = \left\{ \hat{\mathbf{V}}^T \, V_3 \right\}^T$ contains the mid-plane translation components, with $\hat{\mathbf{V}} = \{V_1 \, V_2\}^T$ collecting those lying in the X_1-X_2 plane, and $\mathbf{\Phi} = \{\Phi_1 \, \Phi_2\}^T$ the rotation components of the fiber orthogonal to the mid-plane about direction X_2 and $-X_1$, i.e. the specific positive rotation convention for shell model is adopted.

By applying the compatibility conditions, the 3D strain fields, $\mathbf{\Theta} = \left\{ \hat{\mathbf{\Theta}}^T \, \Theta_{33} \, \mathbf{\Theta}_3^T \right\}^T$, with $\hat{\mathbf{\Theta}} = \{\Theta_{11} \, \Theta_{22} \, \Theta_{12}\}^T$ and $\mathbf{\Theta}_3 = \{\Theta_{13} \, \Theta_{23}\}^T$, are derived as:

$$
\begin{aligned}
\hat{\mathbf{\Theta}} &= \hat{\mathbf{E}} + X_3 \, \mathbf{K} \\
\Theta_{33} &= 0 \\
\mathbf{\Theta}_3 &= \mathbf{\Gamma}
\end{aligned}
\tag{2}
$$

where $\hat{\mathbf{E}} = \{E_{11} \, E_{22} \, \Gamma_{12}\}^T$, $\mathbf{K} = \{K_{11} \, K_{22} \, K_{12}\}^T$ and $\mathbf{\Gamma} = \{\Gamma_{13} \, \Gamma_{23}\}^T$ are the membrane strains, plate curvatures and plate shear strains, respectively. These quantities are arranged in the generalized shell strain

vector $\mathbf{E} = \left\{ \hat{\mathbf{E}}^T \, \mathbf{K}^T \, \mathbf{\Gamma}^T \right\}^T$ and are defined as:

$$\begin{aligned}
\hat{\mathbf{E}} &= \hat{\mathbf{D}}_{\mathbf{X}} \hat{\mathbf{V}} \\
\mathbf{K} &= \hat{\mathbf{D}}_{\mathbf{X}} \mathbf{\Phi} \\
\mathbf{\Gamma} &= \hat{\mathbf{\nabla}}_{\mathbf{X}} V_3 + \mathbf{\Phi}
\end{aligned} \tag{3}$$

where $\hat{\mathbf{D}}_{\mathbf{X}}$ and $\hat{\mathbf{\nabla}}_{\mathbf{X}}$ denote the in-plane compatibility and gradient operator, respectively, at the macroscopic level and result as follows:

$$\hat{\mathbf{D}}_{\mathbf{X}} = \begin{bmatrix} \frac{\partial}{\partial X_1} & 0 \\ 0 & \frac{\partial}{\partial X_2} \\ \frac{\partial}{\partial X_2} & \frac{\partial}{\partial X_1} \end{bmatrix}, \qquad \hat{\mathbf{\nabla}}_{\mathbf{X}} = \left\{ \begin{array}{c} \frac{\partial}{\partial X_1} \\ \frac{\partial}{\partial X_2} \end{array} \right\} \tag{4}$$

Accordingly, the work-conjugate stress quantities are collected in vectors $\mathbf{N} = \{N_{11} \, N_{22} \, N_{12}\}^T$, containing the membrane stresses, $\mathbf{M} = \{M_{11} \, M_{22} \, M_{12}\}^T$, collecting the plate bending and torsional couples, and $\mathbf{Q} = \{Q_{13} \, Q_{23}\}^T$, listing the plate shear forces. Then, the equilibrium equations governing the shell problem are written as:

$$\begin{aligned}
\hat{\mathbf{D}}_{\mathbf{X}}^T \mathbf{N} + \hat{\mathbf{B}} &= \mathbf{0} \tag{5} \\
\hat{\mathbf{D}}_{\mathbf{X}}^T \mathbf{M} + \mathbf{Q} &= \mathbf{0} \tag{6} \\
\hat{\mathbf{\nabla}}_{\mathbf{X}}^T \mathbf{Q} + B_3 &= 0
\end{aligned}$$

where $\hat{\mathbf{B}} = \{B_1 \, B_2\}^T$ contains the thickness resultants of the distributed load components applied along directions X_1 and X_2 and B_3 is the thickness resultant of the distributed load component applied along the orthogonal direction to the shell mid-plane.

The constitutive response at each point of the shell is derived by performing the downscaling, that is by analyzing the response of the UC at the microscale.

2.2. Formulation of the 3D problem at the microscale

The UC selected for the analysis at the microscale level accounts in detail for the real medium geometry and arrangement and is denoted in the following as Ω; it . In particular, the 3D UC illustrated in Figure 1(a) is considered, with dimensions $2\,a_1 \times 2\,a_2 \times t$ and volume $V = A\,t$, with A denoting the area of the UC mid-plane. The Cartesian coordinate system (x_1, x_2, x_3) is introduced with x_1 and x_2 lying in the UC mid-plane and $x_3 \equiv X_3$ along the shell thickness. Mortar joints are here modeled as zero-thickness interfaces between adjacent bricks (Figure 1(b)). Hence, interfaces represent both the mortar and the two adhesion surfaces between bricks and mortar.

As a running bond texture is here considered, mortar joints are parallel to x_1-x_3 plane (bed joints) and x_2-x_3 plane (head joints), with the unit normal vectors resulting as $\mathbf{j} = \{0\,1\,0\}^T$ and $\mathbf{j} = \{1\,0\,0\}^T$, respectively. The 2D domain collecting all the bed joints is denoted by $\Im_b$, while that collecting all the head joints is denoted by $\Im_h$. Thus, the whole domain results $\Omega = \Omega_b \cup \Im_b \cup \Im_h$, being Ω_b the bricks domain.

The 3D model is adopted for the UC, and the displacement fields $\mathbf{u} = \left\{ \hat{\mathbf{u}}^T \, u_3 \right\}^T$, with $\hat{\mathbf{u}} = \{u_1 \, u_2\}^T$, at each point $\mathbf{x} = \left\{ \hat{\mathbf{x}}^T \, x_3 \right\}^T$ of the UC, with $\hat{\mathbf{x}} = \{x_1 \, x_2\}^T$, are represented as the additive composition of an assigned part, $\bar{\mathbf{u}} = \left\{ \hat{\bar{\mathbf{u}}}^T \, \bar{u}_3 \right\}^T$, with $\hat{\bar{\mathbf{u}}} = \{\bar{u}_1 \, \bar{u}_2\}^T$, expressed as function of the macroscopic shell strains, and an unknown contribution $\mathbf{u}^\star = \left\{ \hat{\mathbf{u}}^{\star T} \, u_3^\star \right\}^T$, with $\hat{\mathbf{u}}^\star = \{u_1^\star \, u_2^\star\}^T$, denoted as perturbation fields. Hence,
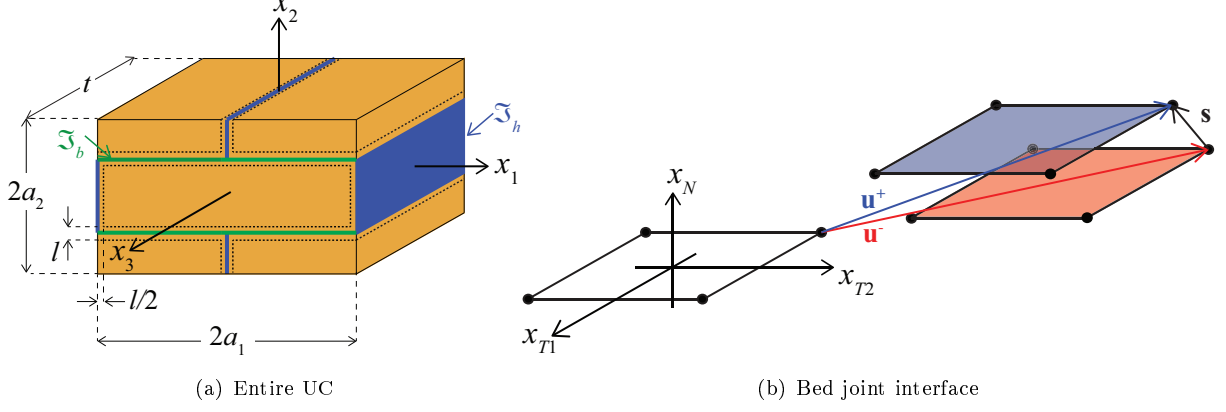
(a) Entire UC (b) Bed joint interface

Figure 1: 3D Unit Cell describing masonry running bond texture.

it is:

$$\mathbf{u}\left(\mathbf{x}\right) = \bar{\mathbf{u}}\left(\mathbf{x}\right) + \mathbf{u}^{*}\left(\mathbf{x}\right) \tag{7}$$

that, explicitly, results as:

$$
\begin{aligned}
u_1\left(x_1, x_2, x_3\right) &= E_{11}x_1 + \frac{1}{2}\Gamma_{12}x_2 + x_3\left(K_{11}x_1 + \frac{1}{2}K_{12}x_2\right) + u_1^{\star}\left(x_1, x_2, x_3\right) \\
u_2\left(x_1, x_2, x_3\right) &= \frac{1}{2}\Gamma_{12}x_1 + E_{22}x_2 + x_3\left(\frac{1}{2}K_{12}x_1 + K_{22}x_2\right) + u_2^{\star}\left(x_1, x_2, x_3\right) \\
u_3\left(x_1, x_2, x_3\right) &= \Gamma_{13}x_1 + \Gamma_{23}x_2 - \frac{1}{2}\left(K_{11}x_1^2 + K_{22}x_2^2 + K_{12}x_1x_2\right) + u_3^{\star}\left(x_1, x_2, x_3\right)
\end{aligned}
\tag{8}
$$

The introduction of the perturbation fields $\mathbf{u}^{\star}$ allows to simultaneously account for the material heterogeneity and the three-dimensional effects with respect to the shell structural model. These satisfy the following periodicity conditions:

$$
\begin{aligned}
\mathbf{u}^{\star}\left(-a_1, x_2, x_3\right) &= \mathbf{u}^{\star}\left(a_1, x_2, x_3\right) \\
\mathbf{u}^{\star}\left(x_1, -a_2, x_3\right) &= \mathbf{u}^{\star}\left(x_1, a_2, x_3\right)
\end{aligned}
\tag{9}
$$

In Figure 1(b) the typical interface is illustrated. The kinematic descriptors for the zero-thickness interfaces are represented by the displacement jumps, $\mathbf{s} = \left\{\hat{\mathbf{s}}^T\ s_3\right\}^T$, with $\hat{\mathbf{s}} = \left\{s_1\ s_2\right\}^T$, i.e. the relative displacements between the two overlapping faces, defined as:

$$\mathbf{s} = \mathbf{u}^{+} - \mathbf{u}^{-} \tag{10}$$

where the displacements of the points belonging to the positive and negative lips of the interface are denoted as $\mathbf{u}^{+}$ and $\mathbf{u}^{-}$, respectively. Considering the representation form (7), the relative displacements (10) can be written as:

$$\mathbf{s} = \left(\bar{\mathbf{u}}^{+} + \mathbf{u}^{*+}\right) - \left(\bar{\mathbf{u}}^{-} + \mathbf{u}^{*-}\right) = \mathbf{u}^{*+} - \mathbf{u}^{*-} \tag{11}$$

as $\bar{\mathbf{u}}^{+} = \bar{\mathbf{u}}^{-}$, so that the displacement jumps at the interface are only defined by the displacement perturbation. On the other hand, this means that the displacement fields $\mathbf{u}^{*}$ are discontinuous in Ω, as these include the displacement jumps at the interfaces [31].

The compatible strain fields at the microscale, $\boldsymbol{\varepsilon} = \left\{\hat{\boldsymbol{\varepsilon}}^T\ \varepsilon_{33}\ \boldsymbol{\gamma}^T\right\}^T$, are derived from the displacements

6

expressed by (8) in the regions where these are continuous and, in compact form, can be written as:

$$
\begin{aligned}
\hat{\boldsymbol{\varepsilon}} &= \hat{\mathbf{E}} + x_3 \mathbf{K} + \hat{\boldsymbol{\varepsilon}}^\star \\
\varepsilon_{33} &= u_{3,3}^\star \\
\boldsymbol{\gamma} &= \boldsymbol{\Gamma} + \boldsymbol{\gamma}^\star
\end{aligned}
\tag{12}
$$

where $\hat{\boldsymbol{\varepsilon}} = \{\varepsilon_{11}\, \varepsilon_{22}\, \gamma_{12}\}^T$, $\boldsymbol{\gamma} = \{\gamma_{13}\, \gamma_{23}\}^T$, $\hat{\boldsymbol{\varepsilon}}^\star = \{\varepsilon_{11}^\star\, \varepsilon_{22}^\star\, \gamma_{12}^\star\}^T$ and $\boldsymbol{\gamma}^\star = \{\gamma_{13}^\star\, \gamma_{23}^\star\}^T$. Eqs. (12), expressed in components, result as:

$$
\begin{aligned}
\varepsilon_{11} &= E_{11} + x_3 K_{11} + u_{1,1}^\star \\
\varepsilon_{22} &= E_{22} + x_3 K_{22} + u_{2,2}^\star \\
\varepsilon_{33} &= u_{3,3}^\star \\
\gamma_{12} &= \Gamma_{12} + x_3 K_{12} + u_{1,2}^\star + u_{2,1}^\star \\
\gamma_{13} &= \Gamma_{13} + u_{1,3}^\star + u_{3,1}^\star \\
\gamma_{23} &= \Gamma_{23} + u_{2,3}^\star + u_{3,2}^\star
\end{aligned}
\tag{13}
$$

$u_{i,j}^\star$ being the derivative of $u_i^\star$ with respect to x_j.

2.3. UC materials constitutive response

A linear elastic constitutive law is assumed for the bricks, so that the stress-strain relationship is written in the classical form:

$$
\boldsymbol{\sigma}^b = \mathbf{C}^b \boldsymbol{\varepsilon} ,
\tag{14}
$$

where $\mathbf{C}^b$ denotes the 6×6 isotropic constitutive matrix.

To reproduce masonry nonlinear response, a damage-friction model is here adopted for interfaces reproducing the response of the mortar joints. In detail, the constitutive model presented in [3] for 2D problems and accounting for damage, sliding friction and unilateral contact is here extended to the 3D framework. To define the constitutive relationship for the interface, it is convenient to introduce the local coordinate system (x_{T1}, x_{T2}, x_N) shown in Figure 1(b), with x_{T1} and x_{T2} lying on the interface plane and x_N denoting the direction normal to it, so that a positive orientation of the unit normal $\mathbf{j}$ is defined. Accordingly, the positive and negative lips of the interface can be identified. The displacement jumps are then expressed with reference to the local coordinate system, i.e. $\mathbf{s} = \{s_{T1}\, s_{T2}\, s_N\}^T$, with s_{T1} and s_{T2} denoting the displacement jumps along the x_{T1} and x_{T2} directions and s_N that in the normal direction x_N.

To define the interface constitutive law, a representative element of area (REA) defined at a lower scale, where a microcrack is located, is linked to the typical point of the interface. The REA area S is subdivided into an undamaged portion, S_u, and a damaged one, S_d. Then, the damage parameter D is defined as the ratio between the damaged and the whole area, i.e. $D = S_d/S$.

The tractions in the undamaged area S_u, $\mathbf{t}^u$, are related to the displacement jumps by a linear elastic relationship. Those in the damaged area S_d, $\mathbf{t}^d$, are zero when the microcrack is open, while emerge due to the unilateral contact and friction effect when the microcrack is closed. Then, the overall tractions $\mathbf{t}$ result

from the composition of $\mathbf{t}^u$ and $\mathbf{t}^d$, and are expressed as:

$$\mathbf{t} = (1-D)\mathbf{t}^u + D\,\mathbf{t}^d = \mathbf{C}\,(\mathbf{s}-\boldsymbol{\pi}) \tag{15}$$

$$\mathbf{t}^u = \mathbf{C}\,\mathbf{s} \tag{16}$$

$$\mathbf{t}^d = \mathbf{C}\,[\mathbf{s} - (\mathbf{c}+\mathbf{p})] \tag{17}$$

where $\mathbf{C}$ is the diagonal matrix collecting the stiffness values in the two tangential, C_{T1}, C_{T2}, and normal, C_N, directions to the interface. In the following, it is assumed an isotropic response of the interface in its plane, so that $C_{T1} = C_{T2} = C_T$. The inelastic vector $\boldsymbol{\pi}$ is defined as:

$$\boldsymbol{\pi} = D\,(\mathbf{c}+\mathbf{p}) \tag{18}$$

where the two contributions $\mathbf{c}$ and $\mathbf{p}$ are the contact and sliding friction displacement jump vectors, respectively. These account for the unilateral contact and sliding friction phenomena and are defined as:

$$\mathbf{c} = H(s_N) \left\{ \begin{array}{c} 0 \\ 0 \\ s_N \end{array} \right\}, \qquad \mathbf{p} = \left\{ \begin{array}{c} p_{T1} \\ p_{T2} \\ 0 \end{array} \right\} \tag{19}$$

with $H(s_N)$ denoting the Heaviside function applied to s_N. The evolution of the sliding friction displacement jumps $\mathbf{p}$, occurring only when damage is activated at the interface, is ruled by the classical Coulomb yield function, expressed as:

$$f\left(\mathbf{t}^d\right) = \mu\,t_N{}^d + \sqrt{t_{T1}^d{}^2 + t_{T2}^d{}^2} \tag{20}$$

where μ is the friction coefficient. The two sliding friction displacement jump components, p_{T1} and p_{T2}, evolve according to the following flow rules and Kuhn-Tucker loading-unloading conditions:

$$\dot{p}_{T1} = \dot{\lambda}\frac{\partial f}{\partial t_{T1}^d} \quad, \quad \dot{p}_{T2} = \dot{\lambda}\frac{\partial f}{\partial t_{T2}^d} \tag{21}$$

$$\dot{\lambda} \geq 0, \quad f\left(\mathbf{t}^d\right) \leq 0, \quad \dot{\lambda}f\left(\mathbf{t}^d\right) = 0 \tag{22}$$

The evolution law of the damage variable D induces a linear softening response for the interface under monotonic loading condition. It accounts for the coupling of fracture modes I and II by introducing two variables, η_N and η_T, defined as the ratios between the first cracking relative displacements, s_N^0 and s_T^0, and those corresponding to the full damaged state, s_N^f and s_T^f. These result as:

$$\eta_N = \frac{s_N^0}{s_N^f} = \frac{s_N^0\,t_N^0}{2G_{cN}}, \qquad \eta_T = \frac{s_T^0}{s_T^f} = \frac{s_T^0\,t_T^0}{2G_{cT}} \tag{23}$$

where t_N^0 and t_T^0 are the peak stresses corresponding to the first cracking relative displacement and G_{cN} and G_{cT} the fracture energies for mode I and II, respectively. The two parameters defined in (23), assuming the same values for the two tangential directions, are properly combined to define parameter η as:

$$\eta = 1 - \frac{1}{\alpha^2}\left(\langle s_N\rangle_+^2\,\eta_N + s_{T1}{}^2\eta_T + s_{T2}{}^2\eta_T\right) \tag{24}$$

where α measures the average displacement jump as:

$$\alpha = \sqrt{\langle s_N\rangle_+^2 + \left(s_{T1}\right)^2 + \left(s_{T2}\right)^2} \tag{25}$$

$\langle s_N \rangle_+$ being the positive part of the normal displacement jump.

The damage associated variable is introduced as:

$$\beta = \sqrt{\left(\frac{\langle s_N \rangle_+}{s_N^0}\right)^2 + \left(\frac{s_{T1}}{s_T^0}\right)^2 + \left(\frac{s_{T2}}{s_T^0}\right)^2} - 1 \tag{26}$$

so that, damage evolves according to the following irreversible law:

$$D = \max_{history} \left\{0, \min\left\{1, \tilde{D}\right\}\right\} \qquad \text{with } \tilde{D} = \frac{1}{\eta}\left(\frac{\beta}{1+\beta}\right) \tag{27}$$

2.4. Linking of micro and macro scales

According to the fundamental rules of the homogenization techniques, average conditions relate the microscopic and macroscopic strain quantities. As for the microscopic components in $\hat{\varepsilon}$, their averages result:

$$\overline{\hat{\varepsilon}} = \hat{\mathbf{E}} + \frac{1}{V}\left[\int_{\Omega_b} \hat{\mathbf{D}}_{\mathbf{x}}\hat{\mathbf{u}}^\star \, dV + \int_{\Im_h \cup \Im_b} \mathbf{J}\hat{\mathbf{s}} \, d\Im\right] \tag{28}$$

where $\hat{\mathbf{D}}_{\mathbf{x}}$ is the compatibility operator referred to the microscale Cartesian coordinates x_1 and x_2, i.e. $\hat{\varepsilon}^\star = \hat{\mathbf{D}}_{\mathbf{x}}\hat{\mathbf{u}}^\star$. Matrix $\mathbf{J}$ collects the first two components of the unit vector $\mathbf{j}$ normal to the interface, that is:

$$\mathbf{J} = \begin{bmatrix} j_1 & 0 \\ 0 & j_2 \\ j_2 & j_1 \end{bmatrix} \tag{29}$$

Eq. (28), written in components, results as:

$$\begin{aligned}
\overline{\varepsilon}_{11} &= E_{11} + \frac{1}{V}\left[\int_{\Omega_b} u^\star_{1,1} \, dV + \int_{\Im_h} s_1 \, dx_2 \, dx_3\right] \\
\overline{\varepsilon}_{22} &= E_{22} + \frac{1}{V}\left[\int_{\Omega_b} u^\star_{2,2} \, dV + \int_{\Im_b} s_2 \, dx_1 \, dx_3\right] \\
\overline{\gamma}_{12} &= \Gamma_{12} + \frac{1}{V}\left[\int_{\Omega_b} \left(u^\star_{1,2} + u^\star_{2,1}\right) dV + \int_{\Im_b} s_1 \, dx_1 \, dx_3 + \int_{\Im_h} s_2 \, dx_2 \, dx_3\right]
\end{aligned} \tag{30}$$

To satisfy the average condition requiring that the average of the microscopic components must be equal to the corresponding macroscopic quantities, the terms in the brackets in Eq. (28), or equivalently in Eqs. (30), need to vanish, that is:

$$\int_{\Omega_b} \hat{\mathbf{D}}_{\mathbf{x}}\hat{\mathbf{u}}^\star \, dV + \int_{\Im_h \cup \Im_b} \mathbf{J}\hat{\mathbf{s}} \, d\Im = \mathbf{0} \tag{31}$$

As a consequence of the periodic nature of the perturbation displacement components $u_1^\star$ and $u_2^\star$, Eq. (31) is automatically satisfied.

The evaluation of the equivalent curvatures at the microscale requires the definition of the equivalent rotations, $\boldsymbol{\phi} = \{\phi_1 \, \phi_2\}^T$, of the fibers orthogonal to the UC mid-plane. Displacement vector $\hat{\mathbf{u}}$, collecting the components along x_1 and x_2, can be decomposed into two terms:

$$\hat{\mathbf{u}} = \hat{\mathbf{u}}^r + \hat{\mathbf{u}}^d \tag{32}$$

9

where $\hat{\mathbf{u}}^r$ are the rigid displacements of the fiber orthogonal to the wall mid-plane, represented in the form:

$$\hat{\mathbf{u}}^r = \hat{\mathbf{v}} + x_3\boldsymbol{\phi} \tag{33}$$

Term $\hat{\mathbf{v}}$ collects the in-plane displacement components of the points lying in the UC mid-plane, that is at $x_3 = 0$ and $\boldsymbol{\phi} = \{\phi_1\,\phi_2\}^T$ describes the rigid rotation of the fiber. Note that $\hat{\mathbf{v}}$ and $\boldsymbol{\phi}$ are functions only of the in-plane coordinates x_1 and x_2. In order to enforce that the rigid displacements $\hat{\mathbf{u}}^r$ be the better linear approximation of the displacement fields $\hat{\mathbf{u}}$, a least square minimization problem can be stated in the form:

$$\min_{\hat{\mathbf{v}},\boldsymbol{\phi}} \int_{-t/2}^{t/2} [\hat{\mathbf{u}} - \hat{\mathbf{u}}^r\,(\hat{\mathbf{v}},\boldsymbol{\phi})]^2\,dx_3 \tag{34}$$

By solving problem (34) and accounting for Eqs. (32) and (33) the following conditions are derived:

$$\int_{-t/2}^{t/2} \hat{\mathbf{u}}^d\,dx_3 = \mathbf{0}, \qquad \int_{-t/2}^{t/2} x_3\hat{\mathbf{u}}^d\,dx_3 = \mathbf{0} \tag{35}$$

leading to:

$$\hat{\mathbf{v}} = \frac{1}{t} \int_{-t/2}^{t/2} \hat{\mathbf{u}}\,dx_3, \qquad \boldsymbol{\phi} = \frac{12}{t^3} \int_{-t/2}^{t/2} x_3\hat{\mathbf{u}}\,dx_3 \tag{36}$$

By introducing Eqs. (8) in the second of Eq. (36) and eliminating the vanishing integral terms, it results in components:

$$\phi_1 = K_{11}x_1 + \frac{1}{2}K_{12}x_2 + \frac{12}{t^3} \int_{-t/2}^{t/2} x_3 u_1^\star\,dx_3 \tag{37}$$

$$\phi_2 = \frac{1}{2}K_{12}x_1 + K_{22}x_2 + \frac{12}{t^3} \int_{-t/2}^{t/2} x_3 u_2^\star\,dx_3 \tag{38}$$

Once the equivalent fiber rotation is determined from the 3D perturbation displacement fields, the microscopic plate curvature vector, $\boldsymbol{\kappa} = \{\kappa_{11}\,\kappa_{22}\,\kappa_{12}\}^T$, is defined as:

$$\boldsymbol{\kappa} = \hat{\mathbf{D}}_{\mathbf{x}}\,\boldsymbol{\phi} \tag{39}$$

Then, by accounting for Eqs. (37) and (38), it results:

$$\boldsymbol{\kappa} = \mathbf{K} + \frac{12}{t^3} \int_{-t/2}^{t/2} x_3\hat{\mathbf{D}}_{\mathbf{x}}\hat{\mathbf{u}}^\star\,dx_3 \tag{40}$$

so that, the average of $\boldsymbol{\kappa}$ evaluated over the UC mid-plane area A, in compact form, reads as:

$$\overline{\boldsymbol{\kappa}} = \mathbf{K} + \frac{12}{At^3} \left[\int_{\Omega_b} x_3\,\hat{\mathbf{D}}_{\mathbf{x}}\hat{\mathbf{u}}^\star\,dV + \int_{\Im_h \cup \Im_b} x_3\,\mathbf{J}\hat{\mathbf{s}}\,d\Im \right] \tag{41}$$

which, written in components, results:

$$\begin{aligned}
\bar{\kappa}_{11} &= K_{11} + \frac{12}{A\,t^3} \left[\int_{\Omega_b} x_3 u_{1,1}^\star\,dV + \int_{\Im_h} x_3\,s_1\,dx_2\,dx_3 \right] \\
\bar{\kappa}_{22} &= K_{22} + \frac{12}{A\,t^3} \left[\int_{\Omega_b} x_3 u_{2,2}^\star\,dV + \int_{\Im_b} x_3\,s_2\,dx_1\,dx_3 \right] \\
\bar{\kappa}_{12} &= K_{12} + \frac{12}{A\,t^3} \left[\int_{\Omega_b} x_3\,(u_{1,2}^\star + u_{2,1}^\star)\,dV + \int_{\Im_b} x_3\,s_1\,dx_1\,dx_3 + \int_{\Im_h} x_3\,s_2\,dx_2\,dx_3 \right]
\end{aligned} \tag{42}$$

To satisfy the average condition for the curvature components, the terms in the brackets at the right-hand-side of Eq. (41), or equivalently of Eqs. (42), need to vanish, i.e.:

$$\int_{\Omega_b} x_3 \, \hat{\mathbf{D}}_{\mathbf{x}} \hat{\mathbf{u}}^\star \, dV + \int_{\Im_h \cup \Im_b} x_3 \, \mathbf{J}\hat{\mathbf{s}} \, d\Im = \mathbf{0} \tag{43}$$

The periodicity conditions (9) automatically imply that Eq. (43) is satisfied.

Finally, the average plate shear strains are evaluated. By considering Eqs. $(13)_{5\text{-}6}$, it results in compact form:

$$\overline{\boldsymbol{\gamma}} \;=\; \boldsymbol{\Gamma} + \frac{1}{V} \left[\int_{\Omega_b} \left(\hat{\mathbf{u}}^\star_{,3} + \hat{\boldsymbol{\nabla}}_{\mathbf{x}} u^\star_3 \right) dV + \int_{\Im_h \cup \Im_b} \hat{\mathbf{j}} s_3 \, d\Im \right] \tag{44}$$

where $\hat{\boldsymbol{\nabla}}_{\mathbf{x}}$ denotes the gradient operator referred to the microscale Cartesian coordinates x_1 and x_2 and $\hat{\mathbf{j}}$ contains the first two components of the unit vector $\mathbf{j}$ normal to the interface. Eq. (44), in components, results:

$$\begin{aligned} \overline{\gamma}_{13} &= \Gamma_{13} + \frac{1}{V} \left[\int_{\Omega_b} \left(u^\star_{1,3} + u^\star_{3,1} \right) dV + \int_{\Im_h} s_3 \, dx_2 \, dx_3 \right] \\ \overline{\gamma}_{23} &= \Gamma_{23} + \frac{1}{V} \left[\int_{\Omega_b} \left(u^\star_{2,3} + u^\star_{3,2} \right) dV + \int_{\Im_b} s_3 \, dx_1 \, dx_3 \right] \end{aligned} \tag{45}$$

To ensure that the averages of the microscopic shear strains are equal to the macroscopic corresponding components, the terms in the brackets of Eq. (44), or equivalently of Eqs. (45), need to vanish. The periodic nature of the displacement component $u^\star_3$ implies that:

$$\int_{\Omega_b} \hat{\boldsymbol{\nabla}}_{\mathbf{x}} u^\star_3 \, dV + \int_{\Im_h \cup \Im_b} \hat{\mathbf{j}} s_3 \, d\Im = \mathbf{0} \tag{46}$$

Then, additional 'non-standard' conditions have to be enforced, resulting as:

$$\int_{\Omega_b} \hat{\mathbf{u}}^\star_{,3} \, dV = \mathbf{0} \tag{47}$$

Relying on the generalized Hill-Mandel principle which can be interpreted as the principle of virtual works for a two scale problem, the shell generalized stresses are derived by enforcing the equivalence of the virtual work at the macroscopic point and the average virtual work measured in the UC, in the form:

$$\delta \hat{\mathbf{E}}^T \mathbf{N} + \delta \mathbf{K}^T \mathbf{M} + \delta \boldsymbol{\Gamma}^T \mathbf{Q} = \frac{1}{A} \int_A \left(\int_{-t/2}^{t/2} \delta \boldsymbol{\varepsilon}^T \boldsymbol{\sigma} \, dx_3 \right) dA \tag{48}$$

where the microscopic stress vector work-conjugate to the microscopic strains $\boldsymbol{\varepsilon}$ is defined as $\boldsymbol{\sigma} = \left\{ \hat{\boldsymbol{\sigma}}^T \, \sigma_{33} \, \boldsymbol{\tau}^T \right\}^T$, with $\hat{\boldsymbol{\sigma}} = \{ \sigma_{11} \, \sigma_{22} \, \sigma_{12} \}^T$ and $\boldsymbol{\tau} = \{ \tau_{13} \, \tau_{23} \}^T$. By introducing the virtual variation of the microscopic strains expressed on the basis of the kinematic map in Eq. (13), the expressions of the generalized shell stresses are derived, resulting:

$$\mathbf{N} = \frac{1}{A} \int_A \int_{-t/2}^{t/2} \hat{\boldsymbol{\sigma}} \, dx_3 \, dA \tag{49}$$

for the membrane components,

$$\mathbf{M} = \frac{1}{A} \int_A \int_{-t/2}^{t/2} x_3 \, \hat{\boldsymbol{\sigma}} \, dx_3 \, dA \tag{50}$$

for the flexural and torsional couples, and:

$$\mathbf{Q} = \frac{1}{A} \int_A \int_{-t/2}^{t/2} \boldsymbol{\tau} \, dx_3 \, dA \tag{51}$$

for the shear forces. To be noted is that only microscopic stresses $\boldsymbol{\sigma}^b$ arising in the bricks are averaged to evaluate the macroscopic stress components, as the interfaces give null contributions. Hence, the generalized shell stresses, all collected in vector $\boldsymbol{\Sigma}$, result as:

$$\boldsymbol{\Sigma} = \left\{ \mathbf{N}^T \, \mathbf{M}^T \, \mathbf{Q}^T \right\}^T = \frac{1}{A} \int_A \int_{-t/2}^{t/2} \mathbf{B}^T(\mathbf{x}) \boldsymbol{\sigma}^b(\mathbf{x}) \, dx_3 \, dA \tag{52}$$

being $\mathbf{B}(\mathbf{x})$ the matrix ruling the macro-micro kinematic map deduced by Eq. (13) and resulting equal to:

$$\mathbf{B}(\mathbf{x}) = \begin{bmatrix} 1 & 0 & 0 & x_3 & 0 & 0 & 0 & 0 \\ 0 & 1 & 0 & 0 & x_3 & 0 & 0 & 0 \\ 0 & 0 & 0 & 0 & 0 & 0 & 0 & 0 \\ 0 & 0 & 1 & 0 & 0 & x_3 & 0 & 0 \\ 0 & 0 & 0 & 0 & 0 & 0 & 1 & 0 \\ 0 & 0 & 0 & 0 & 0 & 0 & 0 & 1 \end{bmatrix} \tag{53}$$

3. TFA-based nonlinear homogenization technique

In this section, the adopted TFA-based nonlinear homogenization technique, properly extended to the case of interfaces modeling mortar joints, is presented. This is an enriched version of the procedure recently proposed in [3] with the aim of studying both the in-plane and out-of-plane behavior of periodic masonry.

In the framework of the multiscale approach, the proposed procedure permits to derive the constitutive macroscopic behavior of the composite material on the basis of the micromechanical response of the representative UC. This is regarded as the assembly of elastic bricks and nonlinear interfaces representing mortar joints. The latter are divided into n_s regions $\mathscr{S}^j$ $(j = 1, ... n_s)$, called 'subsets', where the inelastic phenomena are considered as uniform.

Figure 2 shows a possible arrangement of the subsets with reference to the running bond UC. This subset identification derives from the mechanical response of the cell. As a consequence of the assumed running bond texture, the following periodicity conditions hold in the bed joint domain $\Im_b$:

$$\begin{aligned} \mathbf{s}\left(x_1, -\tfrac{a_2}{2}, x_3\right) &= \mathbf{s}\left(x_1 + a_1, +\tfrac{a_2}{2}, x_3\right) & \forall x_1 \in [-a_1, 0] \,, \forall x_3 \in \left[-\tfrac{t}{2}, \tfrac{t}{2}\right] \\ \mathbf{s}\left(x_1, +\tfrac{a_2}{2}, x_3\right) &= \mathbf{s}\left(x_1 + a_1, -\tfrac{a_2}{2}, x_3\right) & \forall x_1 \in [-a_1, 0] \,, \forall x_3 \in \left[-\tfrac{t}{2}, \tfrac{t}{2}\right] \end{aligned} \tag{54}$$

and in the head joint domain $\Im_h$:

$$\begin{aligned} 2\,\mathbf{s}\left(a_1, x_2, x_3\right) = 2\,\mathbf{s}\left(-a_1, x_2, x_3\right) &= \mathbf{s}\left(0, x_2 - a_2, x_3\right) & \forall x_2 \in \left[0, +\tfrac{a_2}{2}\right] \,, \forall x_3 \in \left[-\tfrac{t}{2}, \tfrac{t}{2}\right] \\ 2\,\mathbf{s}\left(a_1, x_2, x_3\right) = 2\,\mathbf{s}\left(-a_1, x_2, x_3\right) &= \mathbf{s}\left(0, x_2 + a_2, x_3\right) & \forall x_2 \in \left[-\tfrac{a_2}{2}, 0\right] \,, \forall x_3 \in \left[-\tfrac{t}{2}, \tfrac{t}{2}\right] \end{aligned} \tag{55}$$

To be noted is that periodicity of the medium can be described by means of a frame of reference made of two independent vectors, $\mathbf{v}_1$ and $\mathbf{v}_2$, and the mechanical properties of the medium are invariant along any

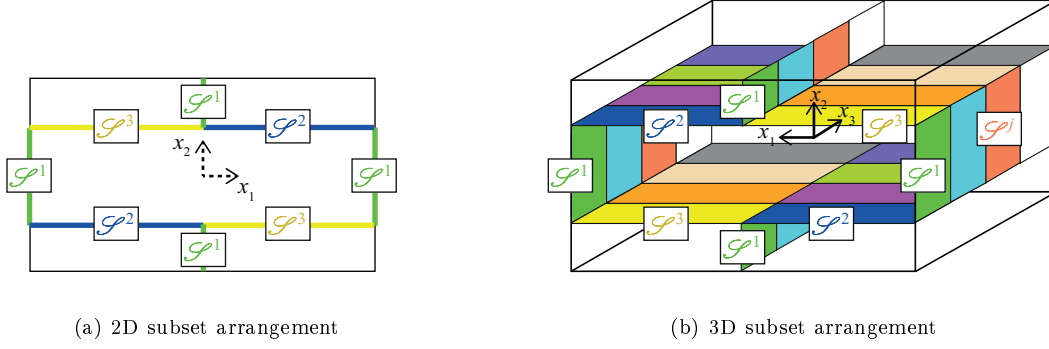(a) 2D subset arrangement (b) 3D subset arrangement

Figure 2: Possible subset identification for a running bond UC.

translation of this frame considering a linear combinations of the two vectors [8]. Then, the frame of reference and the associated cell are not uniquely defined, as evident from Figure 3 where two possible choices are shown. As for the considered masonry arrangement, periodicity is expressed by Eqs. (9), (54) and (55) as well.
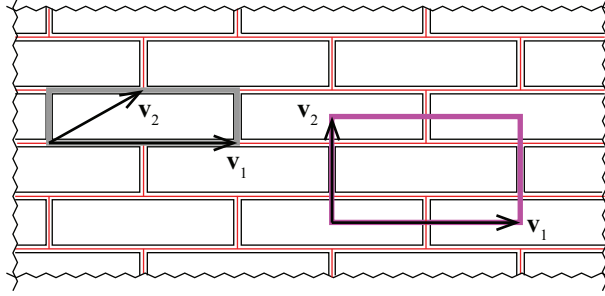

Figure 3: Masonry running bond texture and frame of reference.

If only in-plane loads were applied, three subsets could be considered, i.e. $n_s = 3$, located as shown in Figure 2(a). The first, $\mathscr{S}^1$, collects the head joints, the second, $\mathscr{S}^2$, the bed joints in the positive-positive and negative-negative x_1-x_2 quarters and the third, $\mathscr{S}^3$, the bed joints in the positive-negative and negative-positive x_1-x_2 quarters. However, when out-of-plane loads act and shear-flexural behavior is activated, a through-thickness subdivision is required, as non-uniform behavior is expected through the thickness t. Hence, the number of subsets increases, because of the further discretization required along the x_3 direction. Denoting by n_t the number of independent layers considered along the thickness, the total number of subsets in the UC is equal to $n_s = 3 \times n_t$. The resulting arrangement is shown in Figure 2(b) for $n_t = 4$, so that it results $n_s = 12$. Here, the regions of the UC belonging to the same subset are plotted with the same color.

To be noted is that the proposed procedure is general and can be adopted for any kind of single leaf masonry texture and UC geometry, by identifying the proper subset arrangement.

To determine the macroscopic constitutive behavior, the overall response of the cell is obtained by superimposing two independent contributions: one due to the average strains $\mathbf{E}$ and the other due to the inelastic displacement jumps $\boldsymbol{\pi}^i$ of each subset, with $i = 1, ..., n_s$. Consequently, two sets of linear elastic micromechanical problems have to be solved for the UC under the periodicity conditions in Eq. (9), that is:

a) 8 problems, where one component at time of $\mathbf{E}$ is set equal to 1 while all the others are zeros, considering $\boldsymbol{\pi}^i = \mathbf{0}$, with $i = 1, ..., n_s$

b) $3\,n_s$ problems (3 per each subset), where the components in $\boldsymbol{\pi}^i$ are the input parameters set equal to 1 one at time, with $i = 1, ..., n_s$, considering $\mathbf{E} = \mathbf{0}$ and $\boldsymbol{\pi}^{j \neq i} = \mathbf{0}$, with $j = 1, ..., n_s$.

13

The above linear elastic analyses give as output the localization matrices required to recover local strain, stress and displacement jump values at any point of the UC, when $\mathbf{E}$ and $\boldsymbol{\pi}^i$ are prescribed.

When the average strains $\mathbf{E}$ are applied (set a), the solution of the micromechanical problems allows to compute strains and stresses at the typical point $\mathbf{x}$ of the bricks as:

$$
\begin{array}{rcl}
\varepsilon_{\mathbf{E}}^b\left(\mathbf{x}\right) & = & \mathbf{P}^b\left(\mathbf{x}\right)\mathbf{E} \\
\sigma_{\mathbf{E}}^b\left(\mathbf{x}\right) & = & \mathbf{C}^b\,\mathbf{P}^b\left(\mathbf{x}\right)\mathbf{E}
\end{array}
\tag{56}
$$

and the displacement jumps and tractions at the $j-$th subset $\mathscr{S}^j$ as:

$$
\begin{array}{rcl}
\mathbf{s}_{\mathbf{E}}^j(x_{T1}^j,x_{T2}^j) & = & \mathbf{R}^j(x_{T1}^j,x_{T2}^j)\mathbf{E} \\
\mathbf{t}_{\mathbf{E}}^j(x_{T1}^j,x_{T2}^j) & = & \mathbf{C}^j\,\mathbf{R}^j(x_{T1}^j,x_{T2}^j)\mathbf{E}
\end{array}
\tag{57}
$$

In Eqs. (56) and (57), $\mathbf{P}^b\left(\mathbf{x}\right)$ and $\mathbf{R}^j(x_{T1}^j,x_{T2}^j)$ denote the localization matrix of the strains in the bricks and that of the displacement jumps in the subset $\mathscr{S}^j$, respectively, due to the macroscopic strains $\mathbf{E}$.

When the inelastic displacement jumps $\boldsymbol{\pi}^i$ are prescribed (set b), the resulting strains and stresses at the typical point of the bricks are:

$$
\begin{array}{rcl}
\varepsilon_{\boldsymbol{\pi}^i}^b\left(\mathbf{x}\right) & = & \mathbf{P}_{\boldsymbol{\pi}^i}^b\left(\mathbf{x}\right)\boldsymbol{\pi}^i \\
\sigma_{\boldsymbol{\pi}^i}^b\left(\mathbf{x}\right) & = & \mathbf{C}^b\,\mathbf{P}_{\boldsymbol{\pi}^i}^b\left(\mathbf{x}\right)\boldsymbol{\pi}^i
\end{array}
\tag{58}
$$

and the displacement jumps and tractions at the subset $\mathscr{S}^j$ are:

$$
\begin{array}{rcl}
\mathbf{s}_{\boldsymbol{\pi}^i}^j(x_{T1}^j,x_{T2}^j) & = & \mathbf{R}_{\boldsymbol{\pi}^i}^j(x_{T1}^j,x_{T2}^j)\boldsymbol{\pi}^i \\
\mathbf{t}_{\boldsymbol{\pi}^i}^j(x_{T1}^j,x_{T2}^j) & = & \mathbf{C}^j\left(\mathbf{R}_{\boldsymbol{\pi}^i}^j(x_{T1}^j,x_{T2}^j)-\delta_{ij}\mathbf{I}\right)\boldsymbol{\pi}^i
\end{array}
\tag{59}
$$

In Eqs. (58) and (59), $\mathbf{P}_{\boldsymbol{\pi}^i}^b\left(\mathbf{x}\right)$ and $\mathbf{R}_{\boldsymbol{\pi}^i}^j(x_{T1}^j,x_{T2}^j)$ denote the localization matrix of the strains in the bricks and that of the displacement jumps at the subset $\mathscr{S}^j$, respectively, due to the inelastic strains $\boldsymbol{\pi}^i$, $\mathbf{I}$ is the 3×3 identity matrix, while $\delta_{ij}=1$, if $i=j$, and $\delta_{ij}=0$, if $i\neq j$.

By superimposing the above solutions, displacement jump and traction fields in each subset $\mathscr{S}^j$ result as:

$$
\begin{array}{rcl}
\mathbf{s}^j(x_{T1}^j,x_{T2}^j) & = & \mathbf{R}^j(x_{T1}^j,x_{T2}^j)\mathbf{E}+\displaystyle\sum_{i=1}^{n_s}\mathbf{R}_{\boldsymbol{\pi}^i}^j(x_{T1}^j,x_{T2}^j)\boldsymbol{\pi}^i \\[3mm]
\mathbf{t}^j(x_{T1}^j,x_{T2}^j) & = & \mathbf{C}^j\left[\mathbf{R}^j(x_{T1}^j,x_{T2}^j)\mathbf{E}+\displaystyle\sum_{i=1}^{n_s}\left(\mathbf{R}_{\boldsymbol{\pi}^i}^j(x_{T1}^j,x_{T2}^j)-\delta_{ij}\mathbf{I}\right)\boldsymbol{\pi}^i\right]
\end{array}
\tag{60}
$$

The corresponding average values in the subset $\mathscr{S}^j$ are:

$$
\begin{array}{rcl}
\bar{\mathbf{s}}^j & = & \overline{\mathbf{R}}^j\mathbf{E}+\displaystyle\sum_{i=1}^{n_s}\overline{\mathbf{R}}_{\boldsymbol{\pi}^i}^j\boldsymbol{\pi}^i \\[3mm]
\bar{\mathbf{t}}^j & = & \mathbf{C}^j\left[\overline{\mathbf{R}}^j\mathbf{E}+\displaystyle\sum_{i=1}^{n_s}\left(\overline{\mathbf{R}}_{\boldsymbol{\pi}^i}^j-\delta_{ij}\mathbf{I}\right)\boldsymbol{\pi}^i\right]
\end{array}
\tag{61}
$$

with

$$
\overline{\mathbf{R}}^j=\frac{1}{A^j}\int_{\mathscr{S}^j}\mathbf{R}^j(x_{T1}^j,x_{T2}^j)\,dx_{T1}^j\,dx_{T2}^j\ , \qquad \overline{\mathbf{R}}_{\boldsymbol{\pi}^i}^j=\frac{1}{A^j}\int_{\mathscr{S}^j}\mathbf{R}_{\boldsymbol{\pi}^i}^j(x_{T1}^j,x_{T2}^j)\,dx_{T1}^j\,dx_{T2}^j
\tag{62}
$$

being A^j the total area of all interface portions belonging to subset $\mathscr{S}^j$.

Similarly, strain and stress fields in the bricks result:

$$
\begin{aligned}
\boldsymbol{\varepsilon}^b\left(\mathbf{x}\right) &= \mathbf{P}^b\left(\mathbf{x}\right)\mathbf{E} + \sum_{i=1}^{n_s}\mathbf{P}_{\boldsymbol{\pi}^i}^b\left(\mathbf{x}\right)\boldsymbol{\pi}^i \\
\boldsymbol{\sigma}^b\left(\mathbf{x}\right) &= \mathbf{C}^b\left[\mathbf{P}^b\left(\mathbf{x}\right)\mathbf{E} + \sum_{i=1}^{n_s}\mathbf{P}_{\boldsymbol{\pi}^i}^b\left(\mathbf{x}\right)\boldsymbol{\pi}^i\right]
\end{aligned}
\tag{63}
$$

Finally, by taking into account Eqs. (52) and (63), the generalized shell stress vector $\boldsymbol{\Sigma}$ can be determined as:

$$
\boldsymbol{\Sigma} = \frac{1}{A}\int_A\int_{-t/2}^{t/2}\mathbf{B}^T(\mathbf{x})\mathbf{C}^b\left[\mathbf{P}^b\left(\mathbf{x}\right)\mathbf{E} + \sum_{i=1}^{n_s}\mathbf{P}_{\boldsymbol{\pi}^i}^b\left(\mathbf{x}\right)\boldsymbol{\pi}^i\right]dx_3\,dA = \overline{\mathbf{C}}\mathbf{E} + \sum_{i=1}^{n_s}\overline{\mathbf{C}}_{\boldsymbol{\pi}^i}\boldsymbol{\pi}^i
\tag{64}
$$

with

$$
\overline{\mathbf{C}} = \frac{1}{A}\int_A\int_{-t/2}^{t/2}\mathbf{B}^T(\mathbf{x})\mathbf{C}^b\mathbf{P}^b\left(\mathbf{x}\right)dx_3\,dA\,, \qquad \overline{\mathbf{C}}_{\boldsymbol{\pi}^i} = \frac{1}{A}\int_A\int_{-t/2}^{t/2}\mathbf{B}^T(\mathbf{x})\mathbf{C}^b\mathbf{P}_{\boldsymbol{\pi}^i}^b\left(\mathbf{x}\right)dx_3\,dA
\tag{65}
$$

To be noted is that $\overline{\mathbf{C}}$ represents the equivalent initial elastic stiffness matrix governing the constitutive relation linking the macroscopic shell quantities $\boldsymbol{\Sigma}$ and $\mathbf{E}$.

It is worthwhile remarking that the main limit of TFA technique relies on the a-priori definition of the volume regions, i.e. subsets, where nonlinear phenomena can occur and the assumption of simplified distribution for the nonlinear variables along the subsets. At the same time, this results in a very significant computational savings as shown in the next section illustrating the numerical results.

4. Computational aspects

Computational aspects concerning the evaluation of the solution of the micromechanical problem are discussed in the following.

The finite element (FE) procedure is adopted to perform the 'offline' computations described below and required by the TFA procedure. Moreover, the FE solution of the micromechanical problem is computed and used to validate the proposed TFA approach.

4.1. FE at the microscale

The micromechanical problem described in Sections 2.2 and 2.3 is solved making use of the classical displacement-based 3D FE procedure. The adopted FE procedure is standard for most of the aspects, but some details are required to illustrate how the constraint condition stated by Eq. (47) is managed.

Classical 8-node hexaedral FEs are used to discretize the bricks, while 4+4 zero-thickness quadrilateral FEs are used for the interfaces. The displacement degrees of freedom at node k of the mesh are denoted as $\mathbf{q}_k = \{q_{1k}\,q_{2k}\,q_{3k}\}^T$ and collected in the global vector $\mathbf{q} = \left\{\mathbf{q}_1^T\,\mathbf{q}_2^T...\mathbf{q}_{n_d}^T\right\}^T$, n_d being the number of nodes of the mesh. At the element level, the displacement degrees of freedom are collected in vector $\mathbf{q}^e$, and the following expansions are introduced:

$$
\mathbf{u}^e = \mathbf{N}^e\,\mathbf{q}^e \quad,\quad \boldsymbol{\varepsilon}^e = \mathbf{L}^e\,\mathbf{q}^e \quad,\quad \mathbf{s}^e = \mathbf{H}^e\,\mathbf{q}^e \quad,\quad u_{1,3}^e = \mathbf{G}_1^e\,\mathbf{q}^e \quad,\quad u_{2,3}^e = \mathbf{G}_2^e\,\mathbf{q}^e
\tag{66}
$$

for the element displacement and strain fields of the hexaedral FEs, the displacement jumps at the interface FEs and the derivative with respect to x_3 of the in-plane displacement components, respectively. Matrix $\mathbf{N}^e$ contains the 3D displacement shape functions, $N_1, N_2, \ldots, N_8$, referred to the 8 element nodes, while matrix

$\mathbf{L}^e = \mathbf{D_x}\,\mathbf{N}^e$ contains their derivatives according to the 3D compatibility operator $\mathbf{D_x}$. Matrix $\mathbf{H}^e$ collects the 2D shape functions to evaluate the interface displacement jumps, while $\mathbf{G}_1^e$ and $\mathbf{G}_2^e$ list the derivative of the 8 shape functions with respect to x_3 in the form:

$$\mathbf{G}_1^e = \begin{bmatrix} N_{1,3} & 0 & 0 & N_{2,3} & 0 & 0 & \dots & N_{8,3} & 0 & 0 \end{bmatrix}, \quad \mathbf{G}_2^e = \begin{bmatrix} 0 & N_{1,3} & 0 & 0 & N_{2,3} & 0 & \dots & 0 & N_{8,3} & 0 \end{bmatrix} \tag{67}$$

The equation governing the FE problem at the element level is:

$$\delta\mathbf{q}^{eT}\mathbf{p}^e + \int_{\Omega_b^e} \delta\mathbf{u}^{eT}\mathbf{b}^e \, dV^e = \int_{\Omega_b^e} \delta\boldsymbol{\varepsilon}^{eT}\boldsymbol{\sigma}^e \, dV^e + \int_{\Im_h^e \cup \Im_b^e} \delta\mathbf{s}^{eT}\mathbf{t}^e \, d\Im^e + \int_{\Omega_b^e} \delta\boldsymbol{\lambda}^T \left(\hat{\boldsymbol{u}}_{,3}^{\star e} - \frac{1}{2h}\boldsymbol{\lambda} \right) dV^e \tag{68}$$

with $\mathbf{p}^e$ collecting the internal element nodal forces and $\mathbf{b}^e$ the distributed loads over the FE, which are neglected in the TFA homogenization procedure. The perturbed Lagrangian method [32] is employed to enforce the constraints on the average of $\hat{\mathbf{u}}_{,3}^*$, with $\boldsymbol{\lambda} = \{\lambda_1\,\lambda_2\}^T$ denoting the Lagrange multiplier vector and h the penalty parameter. To be noted is that the additional constraints are only imposed on the FEs discretizing the bricks, as these give rise to vanishing contributions for the interfaces.

By accounting for Eqs. (66), Eq. (68) becomes:

$$\begin{aligned} \delta\mathbf{q}^{eT}\mathbf{p}^e + \delta\mathbf{q}^{eT}\int_{\Omega_b^e}\mathbf{N}^{eT}\mathbf{b}^e \, dV^e &= \delta\mathbf{q}^{eT}\int_{\Omega_b^e}\mathbf{L}^{eT}\boldsymbol{\sigma}^e \, dV^e + \delta\mathbf{q}^{eT}\int_{\Im_h^e \cup \Im_b^e}\mathbf{H}^{eT}\mathbf{t}^e \, d\Im^e \\ &+ \delta\boldsymbol{\lambda}^T\int_{\Omega_b^e}\left\{\begin{array}{c}\mathbf{G}_1^e\mathbf{q}^e \\ \mathbf{G}_2^e\mathbf{q}^e\end{array}\right\} dV^e - \frac{1}{2h}\delta\boldsymbol{\lambda}^T\boldsymbol{\lambda} \end{aligned} \tag{69}$$

By assembling the element contributions, the global virtual work equation is obtained. According to the Newton-Raphson iterative procedure, this is linearized and the following set of equations is derived, governing the micromechanical FE problem:

$$\begin{bmatrix} \mathbf{S}_t^k & \mathbf{g}_1^T & \mathbf{g}_2^T \\ \mathbf{g}_1 & -\dfrac{1}{h} & 0 \\ \mathbf{g}_2 & 0 & -\dfrac{1}{h} \end{bmatrix} \left\{\begin{array}{c} \Delta\mathbf{q}^{k+1} \\ \Delta\lambda_1^{k+1} \\ \Delta\lambda_2^{k+1} \end{array}\right\} = -\left\{\begin{array}{c} \mathbf{R}_q^k \\ R_{\lambda_1}^k \\ R_{\lambda_2}^k \end{array}\right\} \tag{70}$$

where superscript '$k+1$' denotes the current iteration index. Matrices $\mathbf{g}_1$ and $\mathbf{g}_2$ result by assembling the following element contributions:

$$\mathbf{g}_1^e = \int_{\Omega_b^e} \mathbf{G}_1^e \, dV^e \quad, \qquad \mathbf{g}_2^e = \int_{\Omega_b^e} \mathbf{G}_2^e \, dV^e \tag{71}$$

In Eq. (70), $\mathbf{R}_q^k$ denotes the residual of the equilibrium equations, $R_{\lambda_1}^k$ and $R_{\lambda_2}^k$ those of the constraint equations. Finally, $\mathbf{S}_t^k$ is the tangent global stiffness matrix that could result non symmetric because of the non associativity of the interface constitutive law.

The evolution problems of the damage and friction variables governing the interface constitutive response are solved at each of the 2×2 quadrature points located at the interface. To this end, a predictor-corrector algorithm is followed. At the current iteration $k+1$, the displacement jumps at each interface are evaluated. On the basis of these, the damage associated variable β^{k+1} is computed, together with parameter η^{k+1} governing the coupling of fracture modes I and II. Then, the damage variable D^{k+1} is updated. If the interface is affected by the damaging process, the unilateral contact problem and the sliding friction problem are solved, that is the Heaviside function $H\left(s_N^{k+1}\right)$ and the contact vector $\mathbf{c}^{k+1}$ are evaluated. Concerning the sliding friction problem, a prediction-correction technique is implemented. A trial prediction of the sliding friction displacement jumps is computed by setting their values equal to those evaluated at the previous time

step t_n. The trial normal and shear stresses are then evaluated, on the basis of which the trial yield function $f^{k+1,tr}$ is calculated. The correction phase is performed, if $f^{k+1,tr} > 0$. Once the damage, the unilateral contact and the friction problems are solved, the values of the inelastic displacement jumps are updated. The scheme of the described solution algorithm is reported in Table 1.

Table 1: Damage-friction solution procedure for interfaces $\Im_b$ and $\Im_h$.

Iteration '$k+1$'
Damage evaluation
- displacement jumps
$\left\langle s_N^{k+1} \right\rangle_+, \quad s_{T1}^{k+1}, \quad s_{T2}^{k+1}$
- damage associated variable
β^{k+1} (Eq. (26))
- combination parameter of mode I and II
η^{k+1} (Eq. (24))
- damage
D^{k+1} (Eq. (27))
Unilateral effect evaluation
if $s_N^{k+1} \leq 0$ then $H\left(s_N^{k+1}\right) = 0$ else $H\left(s_N^{k+1}\right) = 1$
- inelastic contact vector
$\mathbf{c}^{k+1}$ (Eq. (19))
Sliding friction plasticity evaluation
if $D^{k+1} > 0$
- Prediction phase
$p_{T1}^{k+1,tr} = p_{T1n}$
$p_{T2}^{k+1,tr} = p_{T2n}$
−trial yield function
$f^{k+1,tr} = \mu\, t_N^{d^{k+1,tr}} + \sqrt{\left(t_{T1}^{d^{k+1,tr}}\right)^2 + \left(t_{T2}^{d^{k+1,tr}}\right)^2}$
-check sliding friction
if $f^{k+1,tr} < 0 \Rightarrow \Delta p_{T1}^{k+1} = 0 \,, \Delta p_{T1}^{k+1} = 0$ else
- Correction phase
$\Delta\lambda^{k+1} = \frac{1}{C_T} f^{k+1,tr}$ with
$\Delta\lambda^{k+1} \geq 0 \quad f^{k+1} \leq 0, \quad \Delta\lambda^{k+1}\, f^{k+1} = 0$
$\Delta p_{T1}^{k+1} = \Delta\lambda^{k+1} \dfrac{t_{T1}^{d^{k+1,tr}}}{\sqrt{\left(t_{T1}^{d^{k+1,tr}}\right)^2 + \left(t_{T2}^{d^{k+1,tr}}\right)^2}}$
$\Delta p_{T2}^{k+1} = \Delta\lambda^{k+1} \dfrac{t_{T2}^{d^{k+1,tr}}}{\sqrt{\left(t_{T1}^{d^{k+1,tr}}\right)^2 + \left(t_{T2}^{d^{k+1,tr}}\right)^2}}$

4.2. Numerical procedure for the TFA-based homogenization technique

The nonlinear homogenization technique described in Section 3 requires the evaluation of matrices $\overline{\mathbf{R}}^j$, $\overline{\mathbf{R}}_{\boldsymbol{\pi}^i}^j$, $\overline{\mathbf{C}}$ and $\overline{\mathbf{C}}_{\boldsymbol{\pi}^i}$ ($j = 1, ..., n_s$, $i = 1, ..., n_s$) in Eqs. (62) and (65), which are computed by adopting the FE approach. Thus, the two sets of problems a) and b) described in Section 3 are solved by using the FE micromechanical model. For all analyses, average stresses $\boldsymbol{\Sigma}$ in the UC and average displacement jumps $\bar{\mathbf{s}}^j$ in each subset are computed. These are used to assemble matrices $\overline{\mathbf{C}}$ and $\overline{\mathbf{R}}^j$, respectively, when analyses of set a) are performed, and matrices $\overline{\mathbf{C}}_{\boldsymbol{\pi}^i}$ and $\overline{\mathbf{R}}_{\boldsymbol{\pi}^i}^j$, respectively, when analyses of set b) are carried out. All the analysis performed to solve problems a) and b) are called offline and executed before starting the nonlinear evolutive analysis of the UC.

Once these matrices are determined, the macroscopic response of the UC is evaluated through a strain driven procedure, i.e. for a given history of the macroscopic strains $\mathbf{E}$, the corresponding macroscopic stresses $\boldsymbol{\Sigma}$ is computed through Eq. (64). To be noted is that this depends on the inelastic displacement

jumps $\boldsymbol{\pi}^i$, whose evaluation requires to perform an iterative elastic predictor - inelastic corrector procedure. The damage and unilateral contact-friction evolution problems are, then, solved in each subset $\mathscr{S}^i$, and the inelastic displacement jumps $\boldsymbol{\pi}^i$ are computed. It is assumed that the evolution of damage and sliding friction depend on the average displacement jumps $\bar{\mathbf{s}}^i$, which, in turn, depend on the prescribed overall strains $\mathbf{E}$ and the inelastic displacement jumps of all subsets, as it is clear from Eq. (61). Consequently, the evolution problems of damage and sliding friction variables in all subsets result coupled and a proper solution algorithm has to be employed. In this study, in the spirit of the splitting method, an iterative procedure is adopted by solving a set of n_s uncoupled evolution problems.

Table 2 summarizes the main steps of the developed solution algorithm. Subscript 'n' and superscripts 'k' and '$k+1$' indicate quantities evaluated at the previous time step t_n of the global analysis and at the previous and current iteration of the iterative procedure, respectively.

At the first iteration, '0', considering the inelastic jumps as frozen at the previous time t_n, i.e. $\boldsymbol{\pi}^{j,0} = \boldsymbol{\pi}_n^j$, the average displacement jumps $\bar{\mathbf{s}}^{j,0}$ are evaluated in each subset. These are used as input to solve the evolution problems of damage and sliding friction according to Table 1 and the inelastic displacement jumps $\boldsymbol{\pi}^j$ are updated. Thus, a further iteration is performed by solving again damage, unilateral contact and sliding friction problems in all subsets and the procedure goes on until a convergence test is satisfied. In detail, a residual error is evaluated on the basis of the displacement jumps at the current, previous and first iteration. If this error is lower than a given tolerance, the iterative procedure is stopped and the shell stress vector $\boldsymbol{\Sigma}$ is computed according to Eq. (64), thus providing the homogenized response of the UC in terms of $\boldsymbol{\Sigma}$ and $\mathbf{E}$.

Table 2: Solution algorithm for the TFA procedure.

Iterative solution procedure
1. macroscopic strain vector $\quad$ $\mathbf{E}$ given
2. initialize damage, inelastic contact and sliding friction dispacement jumps in each subset $\mathscr{S}^j$ $\quad$ $D^{j,0} = D_n^j,\ \mathbf{c}^{j,0} = \mathbf{c}_n^j,\ \mathbf{p}^{j,0} = \mathbf{p}_n^j$
3. initialize the inelastic vector in each subset $\mathscr{S}^j$ $\quad$ $\boldsymbol{\pi}^{j,0} = \boldsymbol{\pi}_n^j$
4. localize the displacement jumps in each subset $\mathscr{S}^j$ $\quad$ $\bar{\mathbf{s}}^{j,k+1} = \bar{\mathbf{s}}^{j,0}$ (Eq. $(61)_1$)
5. evaluate damage, inelastic contact and sliding friction dispacement jumps in each subset $\mathscr{S}^j$ $\quad$ $\mathbf{s}^{j,k+1} = \bar{\mathbf{s}}^{j,k+1} \quad \rightarrow \quad D^{j,k+1},\ \mathbf{c}^{j,k+1},\ \mathbf{p}^{j,k+1}$ (Table 1)
6. update inelastic displacement jumps in each subset $\mathscr{S}^j$ $\quad$ $\boldsymbol{\pi}^{j,k+1}$ (Eq. (18))
7. update displacement jumps in each subset $\mathscr{S}^j$ $\quad$ $\bar{\mathbf{s}}^{j,k+1}$ (Eq. $(61)_1$)
8. compute residual $\quad$ $\rho = \sqrt{\dfrac{\sum_j^{n_s} |\bar{\mathbf{s}}^{j,k+1} - \bar{\mathbf{s}}^{j,k}|^2}{\sum_j^{n_s} |\bar{\mathbf{s}}^{j,0}|^2}}$ $\quad$ if $\rho > tol \ \Rightarrow$ go to 5
8. evaluate the generalized shell stress vector $\quad$ $\boldsymbol{\Sigma}$ (Eq. (64))

5. Numerical results

This section presents the numerical results obtained by applying the proposed TFA procedure to study the response of the running bond UC in Figure 1 with dimensions $2a_1 = 250\,\text{mm}$, $2a_2 = 140\,\text{mm}$, $t = 120\,\text{mm}$, block size equal to $240\,\text{mm} \times 60\,\text{mm} \times 120\,\text{mm}$ and mortar layer thickness equal to $l = 10\,\text{mm}$. The material mechanical parameters are those contained in Table 3. Here, $E_{b/m}$ and $G_{b/m}$ denote Young's and shear modulus of brick and mortar, respectively; g_{cN} and g_{cT} are the mode I and II fracture energy densities governing the mortar nonlinear behavior. The corresponding quantities referred to the interface elements are evaluated on the basis of the mortar joint thickness $\hat{l}$, i.e. $C_N = E_m/\hat{l}$, $C_T = G_m/\hat{l}$, $G_{cN} = g_{cN} \times \hat{l}$ and $G_{cT} = g_{cT} \times \hat{l}$, being $\hat{l} = l/2$ for interface elements representing head joints located at the UC boundary and $\hat{l} = l$ otherwise (see Figure 1). To be noted is that the adoption of previous expression for C_N corresponds to uniaxial stress state behavior of the mortar joint. For thin enough and/or large enough joints, confinement of the mortar can influence the joint response and lead to actual stiffer behavior, because of the Poisson effect. Indeed, assuming perfect confinement of the mortar, the adopted value for C_N should be multiplied for a factor that ranges from 1.02 to 1.06 for $\nu = 0.1$ to $\nu = 0.15$ (classical values for the mortar), respectively. Taking into account of the uncertainty of the mortar joint thickness, a good practice is to calibrate C_N from experimental tests where assemblages of bricks and mortar joints like those adopted in the real structural member are studied (see for instance [2]).

Table 3: Material parameters for bricks and mortar.

E_b [MPa]	G_b [MPa]	E_m [MPa]	G_m [MPa]	t_N^0 [MPa]	t_T^0 [MPa]	g_{cN} [MPa]	g_{cT} [MPa]	μ [-]
18000	7826.09	1000	434.78	0.500	0.435	1.25×10^{-3}	2.17×10^{-3}	0.5

The subset arrangement chosen for the proposed TFA procedure is that shown in Figure 2. However, six values of n_t are considered for the layer subdivision across the UC thickness, i.e. $n_t = 1, 2, 4, 6, 8, 10$, maintaining the same subset arrangement in the x_1-x_2 plane (Figure 2(a)).

As described in Section 3, the inelastic displacement jumps and, hence, the damage and friction slip are assumed to be uniform within each subset. In the following, the validity of this assumption is investigated by comparing the TFA solution with that obtained by adopting the FE micromechanical model. For the micromechanical model, blocks and mortar layers are independently modeled through linear elastic brick FEs and nonlinear interfaces, respectively. The FE mesh assumed for the micromechanical model is plotted in Figure 4, where bricks and interfaces are depicted in red and green, respectively.

To be noted is that, as zero-thickness interfaces are adopted, bricks are resized to correctly model the UC texture. Hence, a modified value of bricks elastic modulus should be adopted to take into account the expanded area of blocks. However, no modifications have been made in this work, as not significant differences emerge.

As first step, matrices $\overline{\mathbf{C}}$, $\overline{\mathbf{C}}_{\pi^i}$, $\overline{\mathbf{R}}^j$, $\overline{\mathbf{R}}_{\pi^i}^j$, with $i = 1, ..., n_s$ and $j = 1, ..., n_s$ are computed according to the offline procedure described in Section 4.2, that is by adopting the same FE micromechanical model in Figure 4, yet considering a total of sixteen and twenty FEs along direction x_3 for $n_t = 8$ and $n_t = 10$, respectively, (two FEs per each subset) and twelve FEs for all other cases.

The overall orthotropic elastic matrix does not depend on the number of layers n_t, but depends on the FE mesh adopted for the preliminary elastic analyses. For that reported in Figure 4, it results (units in N and
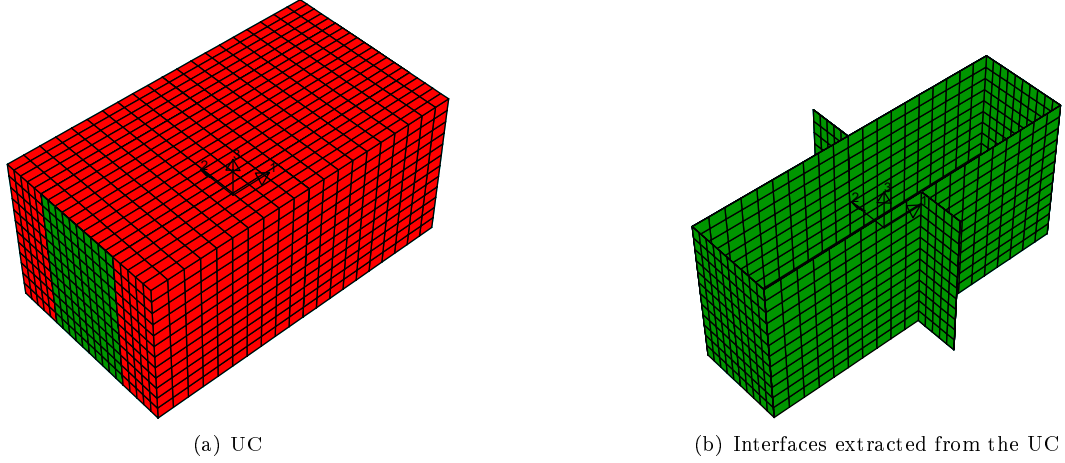
(a) UC

(b) Interfaces extracted from the UC

Figure 4: FE model adopted for micromechanical analyses.

mm):

$$
\overline{\mathbf{C}} = \begin{bmatrix}
1395554 & 58607 & 0.00 & 0.00 & 0.00 & 0.00 & 0.00 & 0.00 \\
58607 & 607199 & 0.00 & 0.00 & 0.00 & 0.00 & 0.00 & 0.00 \\
0.00 & 0.00 & 235522 & 0.00 & 0.00 & 0.00 & 0.00 & 0.00 \\
0.00 & 0.00 & 0.00 & 1743143680 & 73488602 & 0.00 & 0.00 & 0.00 \\
0.00 & 0.00 & 0.00 & 73488602 & 730798248 & 0.00 & 0.00 & 0.00 \\
0.00 & 0.00 & 0.00 & 0.00 & 0.00 & 371686681 & 0.00 & 0.00 \\
0.00 & 0.00 & 0.00 & 0.00 & 0.00 & 0.00 & 262929 & 0.00 \\
0.00 & 0.00 & 0.00 & 0.00 & 0.00 & 0.00 & 0.00 & 635344
\end{bmatrix}
\tag{72}
$$

Figures 5 to 7 show the total deformed configuration of the UC, i.e. that resulting from the total displacement fields $\mathbf{u}(\mathbf{x})$, obtained when $n_t = 4$ for analysis of set a), while Figures 8 to 10 show that obtained for the analysis of set b) when the inelastic displacement jumps at the first three subsets are prescribed. Regions of the UC belonging to the same subset are plotted with the same color, as in Figure 2.

(a) $\hat{\mathbf{E}} = \{1\ 0\ 0\}^T$

(b) $\hat{\mathbf{E}} = \{0\ 1\ 0\}^T$
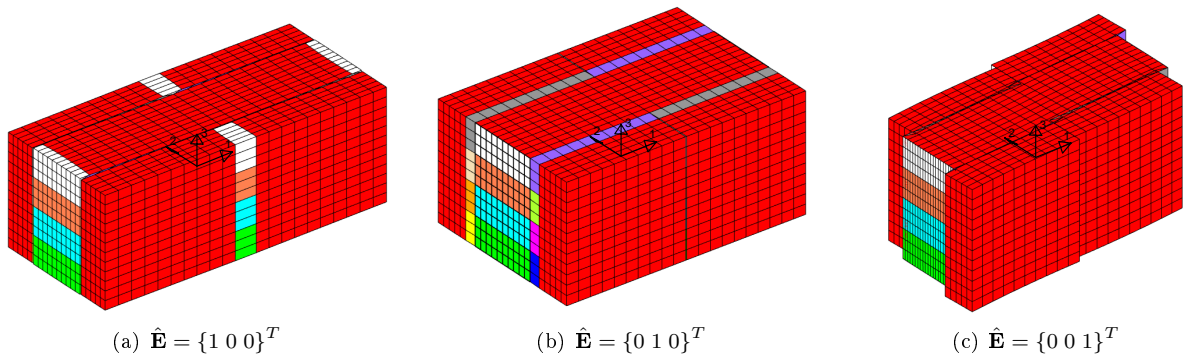

(c) $\hat{\mathbf{E}} = \{0\ 0\ 1\}^T$

Figure 5: UC total deformed configurations obtained by applying the average strains in $\hat{\mathbf{E}}$, with $\mathbf{K} = \mathbf{0}$ and $\mathbf{\Gamma} = \mathbf{0}$ (displacement scale factor equal to 0.25).

After computation of matrices $\overline{\mathbf{C}}$, $\overline{\mathbf{C}}_{\pi^i}$, $\overline{\mathbf{R}}^j$, $\overline{\mathbf{R}}^j_{\pi^i}$, the nonlinear behavior of the UC is investigated, distinguishing the in-plane (membrane) response, involving strain components in $\hat{\mathbf{E}}$, and the out-of-plane (plate) bending and shear responses, involving strain components in $\mathbf{K}$ and $\mathbf{\Gamma}$, respectively. In particular, eight types of loading histories (LH) are considered. These impose different combinations of the total average strain components in $\mathbf{E}$, as reported in Table 4, where a single value indicates that the corresponding quantity is

(a) $\mathbf{K} = \{1\ 0\ 0\}^T$　　　　(b) $\mathbf{K} = \{0\ 1\ 0\}^T$　　　　(c) $\mathbf{K} = \{0\ 0\ 1\}^T$
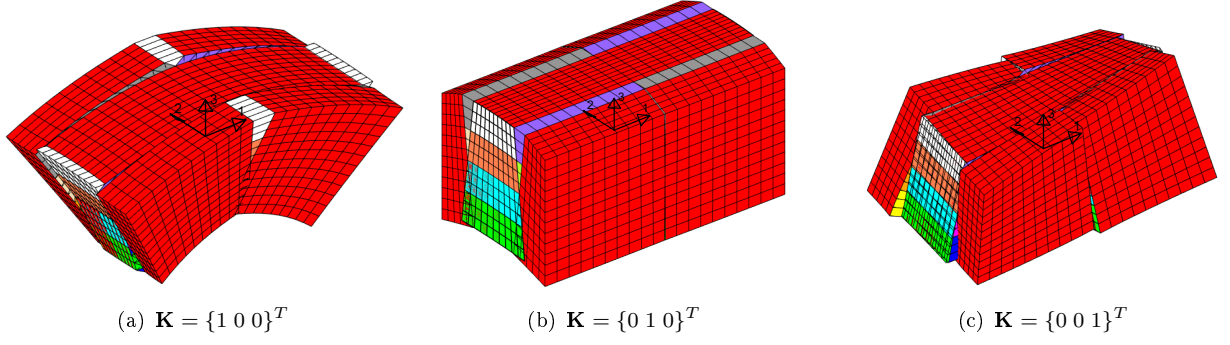
Figure 6: UC total deformed configurations obtained by applying the average strains in $\mathbf{K}$, with $\hat{\mathbf{E}} = \mathbf{0}$ and $\mathbf{\Gamma} = \mathbf{0}$ (displacement scale factor equal to 0.005).
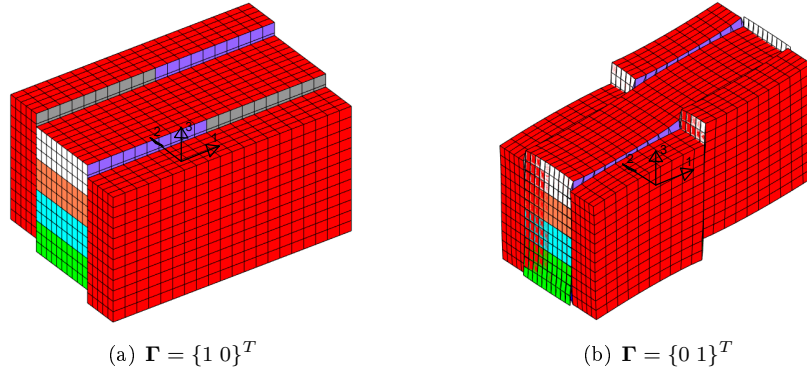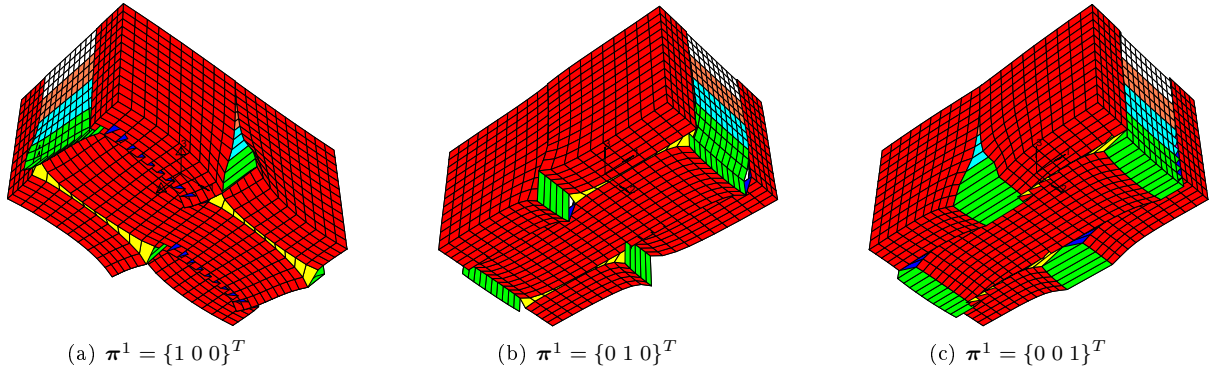

(a) $\mathbf{\Gamma} = \{1\ 0\}^T$　　　　　　(b) $\mathbf{\Gamma} = \{0\ 1\}^T$

Figure 7: UC totoal deformed configurations obtained by applying the average strains in $\mathbf{\Gamma}$, with $\hat{\mathbf{E}} = \mathbf{0}$ and $\mathbf{K} = \mathbf{0}$ (displacement scale factor equal to 0.25).

(a) $\boldsymbol{\pi}^1 = \{1\ 0\ 0\}^T$　　　　(b) $\boldsymbol{\pi}^1 = \{0\ 1\ 0\}^T$　　　　(c) $\boldsymbol{\pi}^1 = \{0\ 0\ 1\}^T$

Figure 8: UC total deformed configurations obtained by applying inelastic displacement jumps $\boldsymbol{\pi}^1$ in subset $\mathscr{S}^1$ (displacement scale factor equal to 100).

kept as constant, while two values separated by symbol '$\rightarrow$' indicate that the corresponding quantity linearly increases according to the indicated range.

5.1. In-plane (membrane) response

LHs 1, 2 and 3 in Table 4 are used to analyze the membrane behavior of the UC. These consider linearly increasing strains E_{11}, E_{22} and Γ_{12}, respectively. For LH 3, a costant value of compressive strain E_{22} is also applied to investigate the influence of sliding friction effects on the UC in-plane shear response.

Figure 11 compares the solution obtained with the TFA procedure (red solid curves) with that computed with the FE micromechanical model (blue dashed curves) for (a) LH 1, i.e. tensile response in the x_1 direction, (b) LH 2, i.e. tensile response in the x_2 direction and (c) LH 3, i.e. shear response under constant
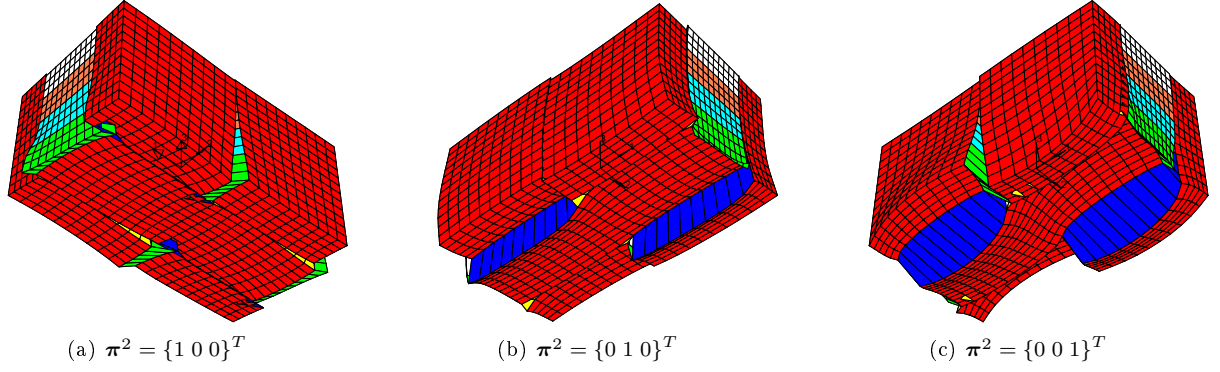
(a) $\boldsymbol{\pi}^2 = \{1\ 0\ 0\}^T$ (b) $\boldsymbol{\pi}^2 = \{0\ 1\ 0\}^T$ (c) $\boldsymbol{\pi}^2 = \{0\ 0\ 1\}^T$

Figure 9: UC total deformed configurations obtained by applying inelastic displacement jumps $\boldsymbol{\pi}^2$ in subset $\mathscr{S}^2$ (displacement scale factor equal to 100).
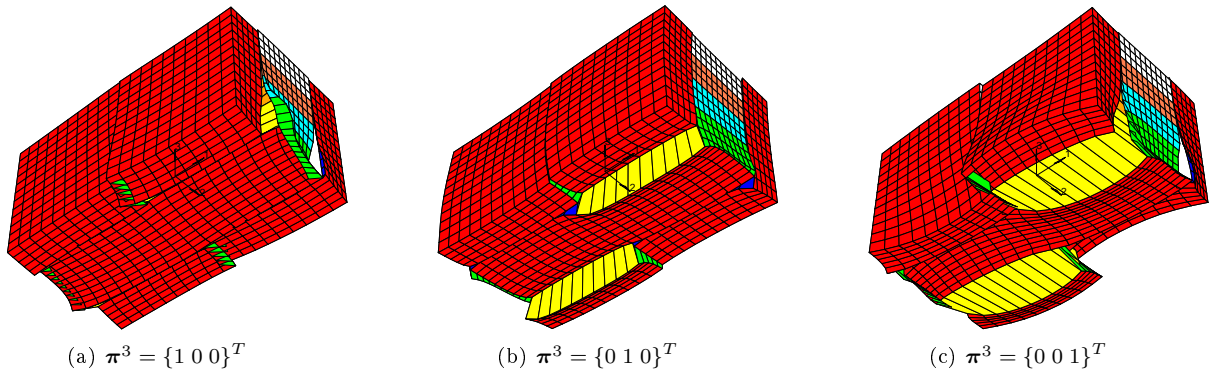

(a) $\boldsymbol{\pi}^3 = \{1\ 0\ 0\}^T$ (b) $\boldsymbol{\pi}^3 = \{0\ 1\ 0\}^T$ (c) $\boldsymbol{\pi}^3 = \{0\ 0\ 1\}^T$

Figure 10: UC total deformed configurations obtained by applying inelastic displacement jumps $\boldsymbol{\pi}^3$ in subset $\mathscr{S}^3$ (displacement scale factor equal to 100).

compressive strain in the x_2 direction. Only the case where $n_t = 1$ is considered for the TFA procedure, as uniform behavior is expected across the UC thickness and, thus, layer subdivision is not required. For all
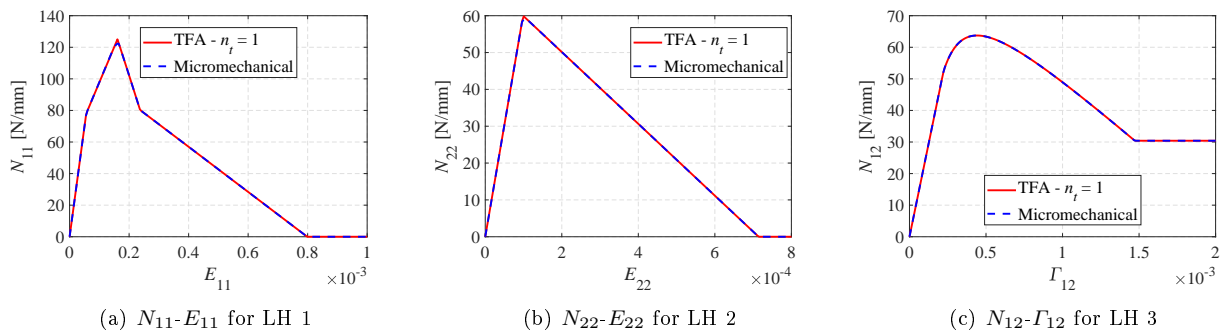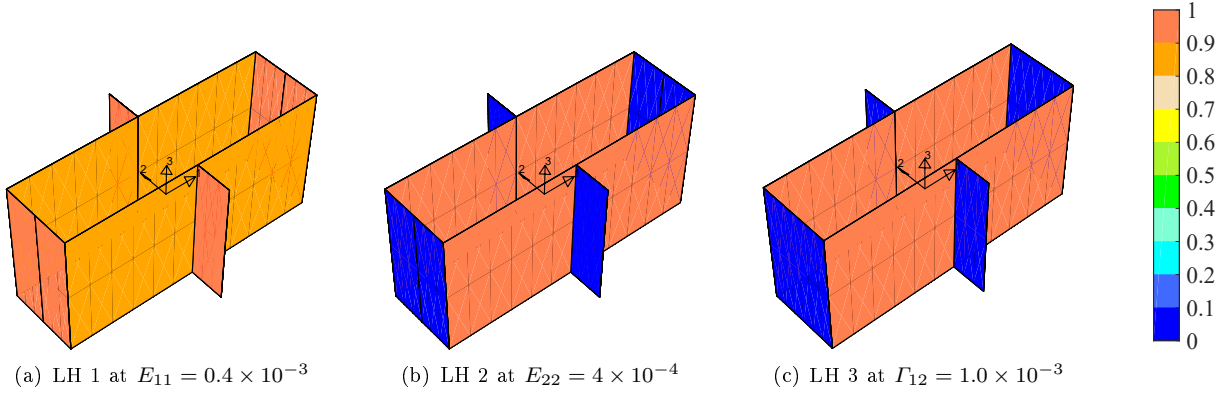

(a) N_{11}-E_{11} for LH 1 (b) N_{22}-E_{22} for LH 2 (c) N_{12}-$\varGamma_{12}$ for LH 3

Figure 11: Average normal and shear stresses N_{11}, N_{22} and N_{12} versus the average strains E_{11}, E_{22} and $\varGamma_{12}$, respectively, for the UC subjected to (a) LH 1, (b) LH 2 and (c) LH 3.

loading conditions, the results obtained with the two models perfectly match proving that the assumption of uniform inelastic jumps inside each subset reasonably holds for these strain states.

This is confirmed by the plots shown in Figures 12 and 13, where damage distributions resulting in the mortar joints for the micromechanical and TFA model, respectively, are depicted. Similar results are found with the TFA 2D-2D procedure proposed in [3].

Table 4: Loading histories considered for the analyses of the UC response.

LH	E_{11}	E_{22}	Γ_{12}	K_{11}	K_{22}	K_{12}	Γ_{23}	Γ_{13}
1	$0 \to e_1$	0	0	0	0	0	0	0
2	0	$0 \to e_2$	0	0	0	0	0	0
3	0	$\bar{e}$	$0 \to e_3$	0	0	0	0	0
4	$0 \to \alpha_1 e_4$	0	0	$0 \to e_4$	0	0	0	0
5	0	$0 \to \alpha_2 e_5$	0	0	$0 \to e_5$	0	0	0
6	$0 \to \alpha_3 e_6$	$0 \to \alpha_3 e_6$	0	0	0	$0 \to e_6$	0	0
7	0	$\bar{e}$	0	0	0	0	$0 \to e_7$	0
8	0	$\bar{e}$	0	0	0	0	0	$0 \to e_8$

$$e_1 = 1.0 \times 10^{-3} \qquad e_2 = 8.0 \times 10^{-4} \qquad e_3 = 2.0 \times 10^{-3} \qquad e_7 = 2.0 \times 10^{-3}$$
$$e_4 = 2.0 \times 10^{-6}\,\text{mm}^{-1} \qquad e_5 = 1.2 \times 10^{-6}\,\text{mm}^{-1} \qquad e_6 = 1.5 \times 10^{-5}\,\text{mm}^{-1} \qquad e_8 = 1.0 \times 10^{-3}$$
$$\bar{e} = -1.0 \times 10^{-4} \qquad \alpha_1 = 0,\, \tfrac{t}{2},\, t \qquad \alpha_2 = \tfrac{t}{2},\, \tfrac{3t}{4},\, t \qquad \alpha_3 = 0,\, \tfrac{t}{8},\, \tfrac{t}{4}$$

(a) LH 1 at $E_{11} = 0.4 \times 10^{-3}$ (b) LH 2 at $E_{22} = 4 \times 10^{-4}$ (c) LH 3 at $\Gamma_{12} = 1.0 \times 10^{-3}$

Figure 12: Distribution of damage variable D resulting at mortar joints obtained with micromechanical model for (a) LH 1, (b) LH 2 and (c) LH 3.

(a) LH 1 at $E_{11} = 0.4 \times 10^{-3}$ (b) LH 2 at $E_{22} = 4 \times 10^{-4}$ (c) LH 3 at $\Gamma_{12} = 1.0 \times 10^{-3}$
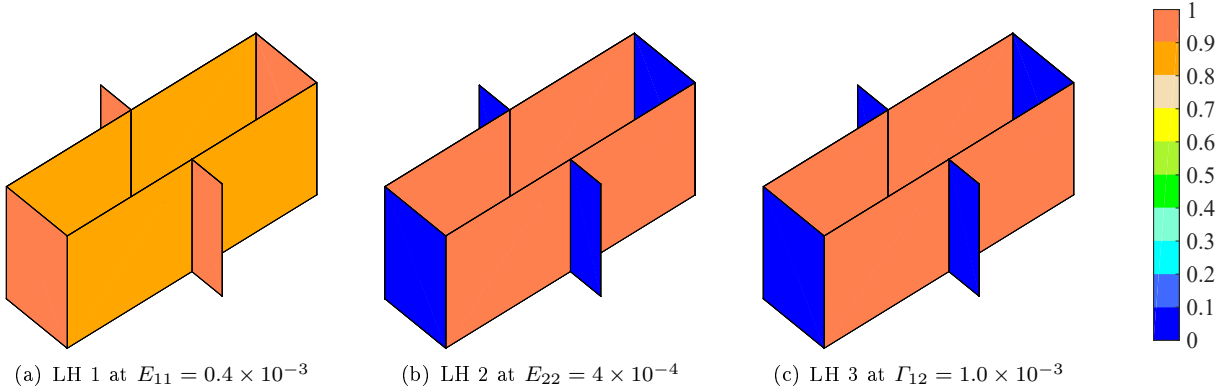
Figure 13: Distribution of damage variable D resulting at mortar joints obtained with TFA approach for (a) LH 1, (b) LH 2 and (c) LH 3.

5.2. Out-of-plane (plate) bending response

LHs 4, 5 and 6 are used to analyze the plate bending behavior of the UC. These consider linearly increasing curvatures K_{11}, K_{22} and K_{12}, respectively. However, to simulate typical tensile-bending strain states occurring in the masonry, plate curvature values are combined with linearly increasing proportional values of the in-plane membrane strains. Coefficients α_1, α_2 and α_3 in Table 4 are used to set the proportionality.

Figure 14 compares the solution obtained with the TFA procedure (solid curves) with that computed with the micromechanical model (dashed curves) for (a) LH 4, i.e. bending around x_2 axis combined with membrane tensile strain in the x_1 direction. TFA solution for $n_t = 2, 4, 6, 8, 10$ are plotted in Figure 14(a),

(a) Influence of the layer number n_t for $\alpha_1 = t$

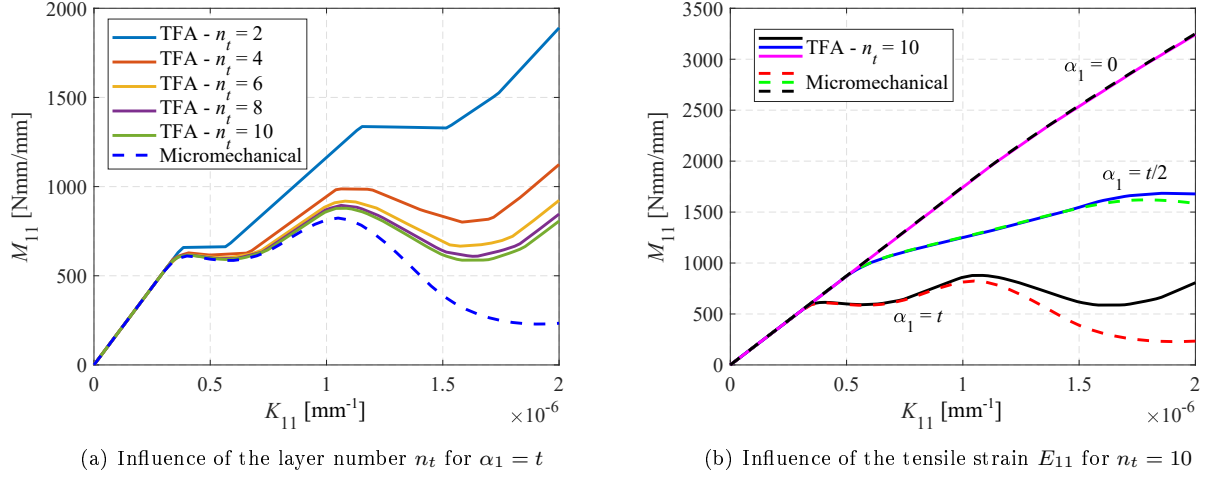(b) Influence of the tensile strain E_{11} for $n_t = 10$

Figure 14: Average bending moment M_{11} versus the average curvature K_{11} for the UC subjected to LH 4.

assuming $\alpha_1 = t$. As shown, two layers suffice to determine the elastic limit strength of the UC, but at least six layers are required to better capture the variation of the nonlinear quantities across the UC thickness. Layer subdivision with $n_t = 4$ can be also used to obtain good approximations of the solution when computational cost needs to be reduced.

To be noted is that, when layer number n_t increases, TFA solution converges to the micromechanical response only for lower values of the bending curvature. For K_{11} greater than 1×10^{-6} mm^{-1}, TFA procedure overestimates the UC strength. This is caused by the particular arrangement of subset assumed in the x_1-x_2 plane (Figure 2). In fact, as shown in Figure 15, when K_{11} exceeds 1×10^{-6} mm^{-1} damage starts growing in the bed joints, assuming a nonuniform distribution in the x_1 direction. By contrast, uniform variation is assumed in the TFA approach, resulting in the damage distributions in Figure 16.

This effect reduces when the tensile strain component E_{11} reduces, as shown in Figure 14(b), where TFA solutions obtained with $n_t = 10$ for three values of the proportional coefficient α_1 are plotted. For $\alpha_1 = t/2$ a perfect match between the models results up to $K_{11} = 1.7 \times 10^{-6}$ mm^{-1}, while for $\alpha_1 = 0$, the entire response curve obtained with TFA procedure coincides with that of the micromechanical model.

(a) $K_{11} = 0.9 \times 10^{-6}$ mm^{-1} (b) $K_{11} = 1.35 \times 10^{-6}$ mm^{-1} (c) $K_{11} = 1.8 \times 10^{-6}$ mm^{-1}
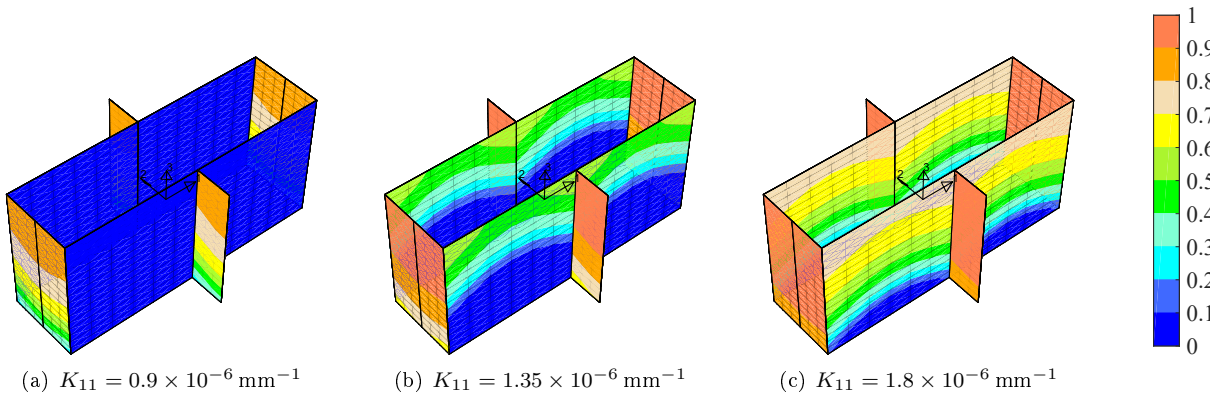
Figure 15: Distribution of damage variable D resulting at mortar joints obtained with micromechanical model for LH 4 and $\alpha_1 = t$.

A different behavior results for bending around x_1 axis combined with membrane tensile strain in the x_2 direction, as shown in Figure 17. This compares the solution obtained with the TFA procedure (solid curves) with that computed with the micromechanical model (dashed curves) for LH 5. As for LH 4, at least four
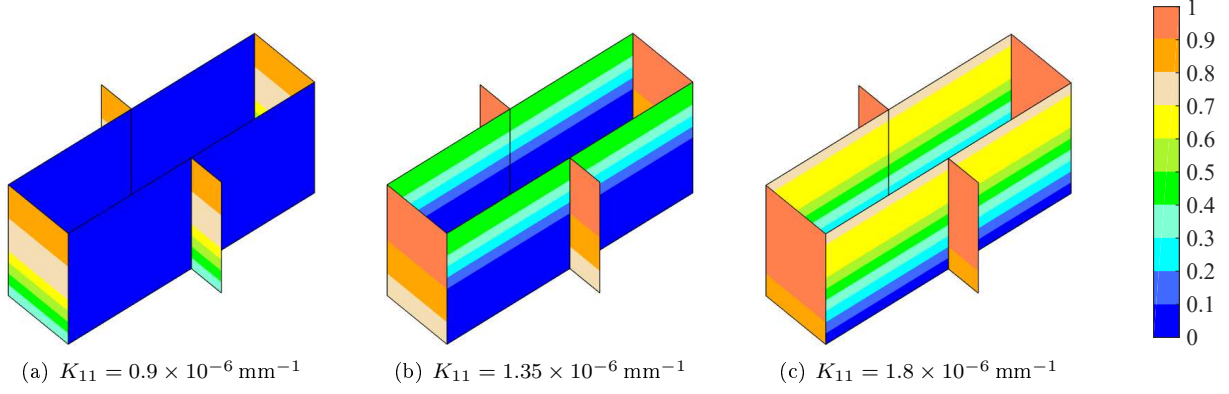
24

(a) $K_{11} = 0.9 \times 10^{-6}\,\mathrm{mm^{-1}}$ (b) $K_{11} = 1.35 \times 10^{-6}\,\mathrm{mm^{-1}}$ (c) $K_{11} = 1.8 \times 10^{-6}\,\mathrm{mm^{-1}}$

Figure 16: Distribution of damage variable D resulting at mortar joints obtained with TFA approach for LH 4, $\alpha_1 = t$ and $n_t = 10$.

layers are required along the UC thickness to obtain satisfactory results (Figure 17(a)). However, when a denser layer subdivision is adopted, the TFA solution always matches that of the micromechanical model, regardless of the value of the tensile strain E_{22} (Figure 17(b)).
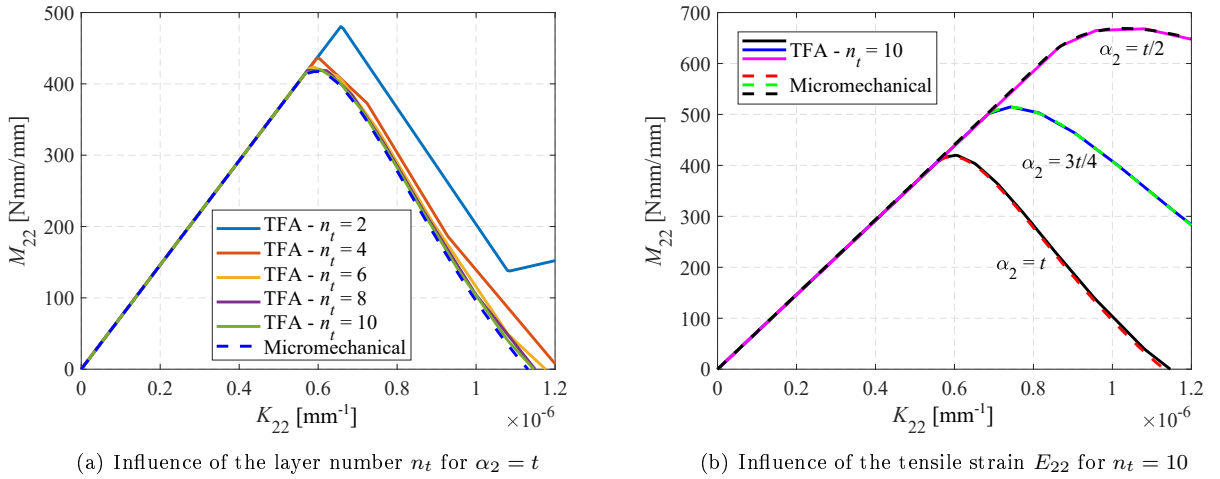
(a) Influence of the layer number n_t for $\alpha_2 = t$ (b) Influence of the tensile strain E_{22} for $n_t = 10$

Figure 17: Average bending moment M_{22} versus the average curvature K_{22} for the UC subjected to LH 5.

In fact, as represented in Figure 18, for this LH, damage occurs only in the bed mortar joints with uniform variation in the x_1 direction. As shown in Figure 19, the subset arrangement chosen for the TFA is able to capture this damage evolution and, thus, to well reproduce the micromechanical response of the UC.

Finally, Figure 20 compares the solution obtained with the TFA procedure (solid curves) with that computed with the micromechanical model (dashed curves) for LH 6, i.e. torsion around x_1 and x_2 axes combined with membrane tensile strains in the x_1 and x_2 directions. Figure 20(a) shows the influence of the layer subdivision for $\alpha_3 = \frac{t}{4}$, while Figure 20(b) shows that of tensile strains E_{11} and E_{22} for $n_t = 10$.

As observed for LH 4, the assumed subset arrangement for the TFA procedure considers only uniform damage variations along the mortar joints, while micromechanical solution shows that nonuniform distributions arise in both bed and head mortar joints (Figures 21 and 22).

Different subset arrangements in the x_1-x_2 plane or nonuniform TFA procedure [29] should be considered to increase model accuracy and capture the nonuniform damage variation along the joints.
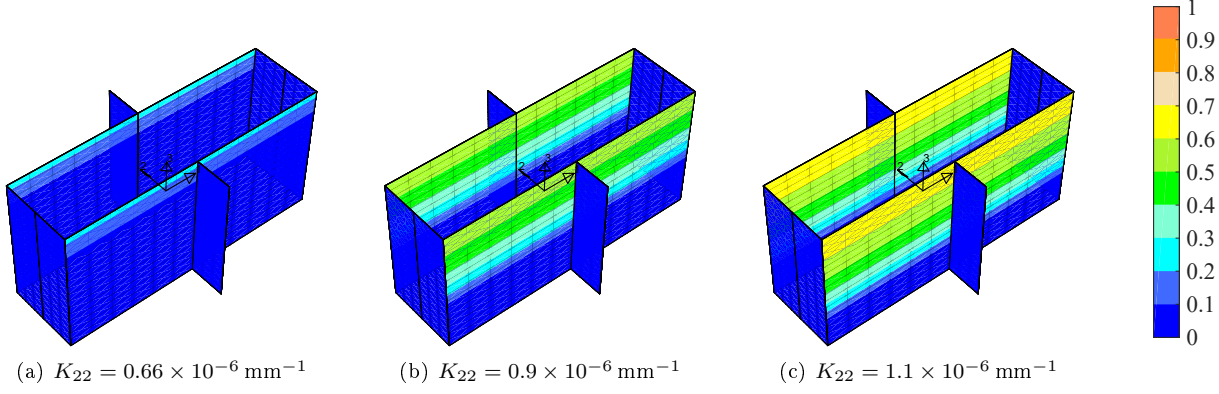
(a) $K_{22} = 0.66 \times 10^{-6}\,\mathrm{mm}^{-1}$ (b) $K_{22} = 0.9 \times 10^{-6}\,\mathrm{mm}^{-1}$ (c) $K_{22} = 1.1 \times 10^{-6}\,\mathrm{mm}^{-1}$

Figure 18: Distribution of damage variable D resulting at mortar joints obtained with micromechanical model for LH 5 and $\alpha_2 = t$.

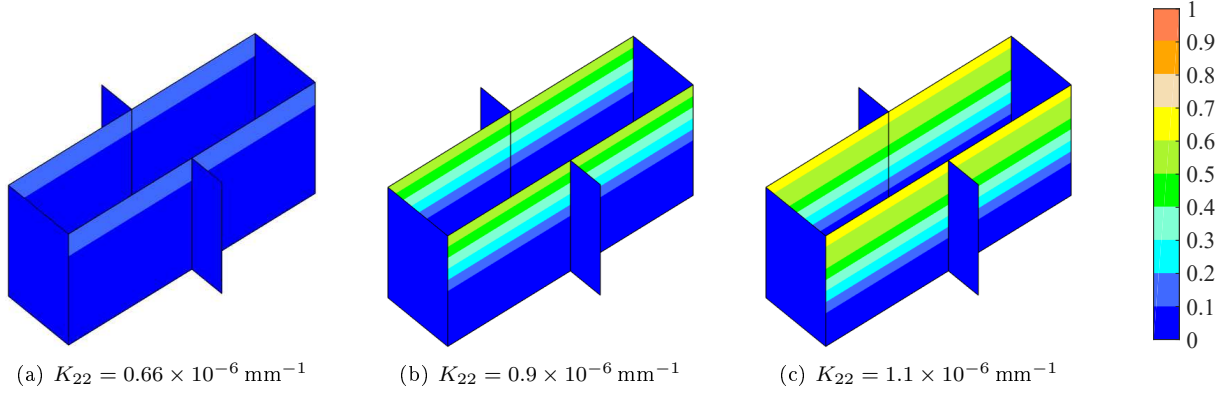(a) $K_{22} = 0.66 \times 10^{-6}\,\mathrm{mm}^{-1}$ (b) $K_{22} = 0.9 \times 10^{-6}\,\mathrm{mm}^{-1}$ (c) $K_{22} = 1.1 \times 10^{-6}\,\mathrm{mm}^{-1}$

Figure 19: Distribution of damage variable D resulting at mortar joints obtained with TFA approach for LH 5, $\alpha_2 = t$ and $n_t = 10$.

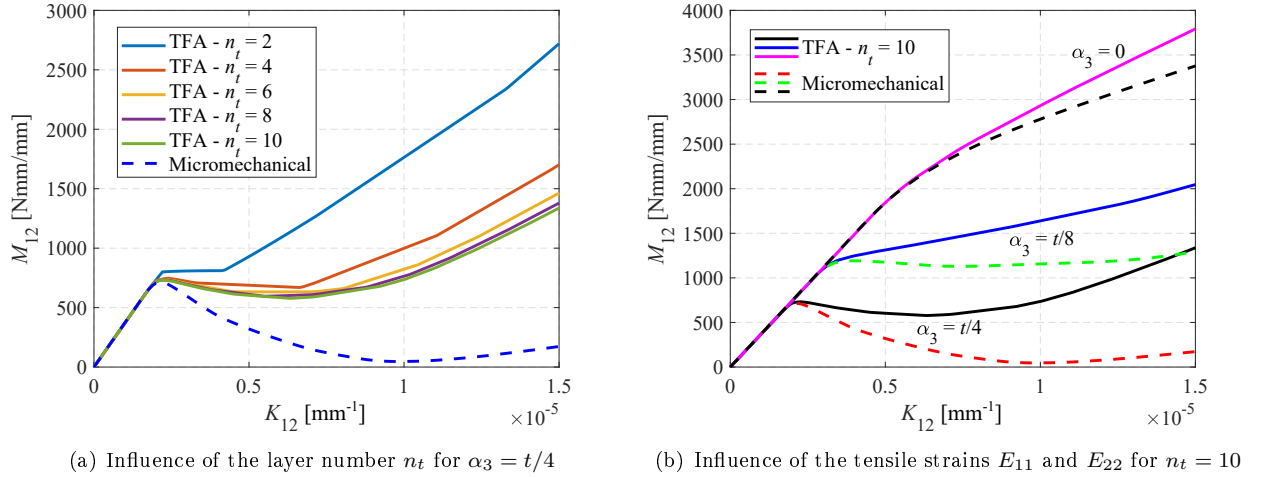(a) Influence of the layer number n_t for $\alpha_3 = t/4$ (b) Influence of the tensile strains E_{11} and E_{22} for $n_t = 10$

Figure 20: Average bending moment M_{12} versus the average curvature K_{12} for the UC subjected to LH 6.

5.3. Out-of-plane (plate) shear response

Finally, LHs 7 and 8 are considered to analyze the plate shear behavior of the UC. These consider linearly increasing shear strains Γ_{23} and Γ_{13}, respectively, while strain E_{22} is fixed to a constant compressive value equal to $\bar{e}$. Figure 23 compares the solution obtained with the TFA procedure (solid curves) with that computed with the micromechanical model (dashed curves) for (a) LH 7, i.e. shear response in the x_2-x_3 plane and (b) LH 8, i.e. shear response in the x_1-x_3 plane. Cases with $E_{22} = 0$ are also plotted, to show

(a) $K_{12} = 0.5 \times 10^{-5}$ mm^{-1} (b) $K_{12} = 1.0 \times 10^{-5}$ mm^{-1} (c) $K_{12} = 1.5 \times 10^{-5}$ mm^{-1}
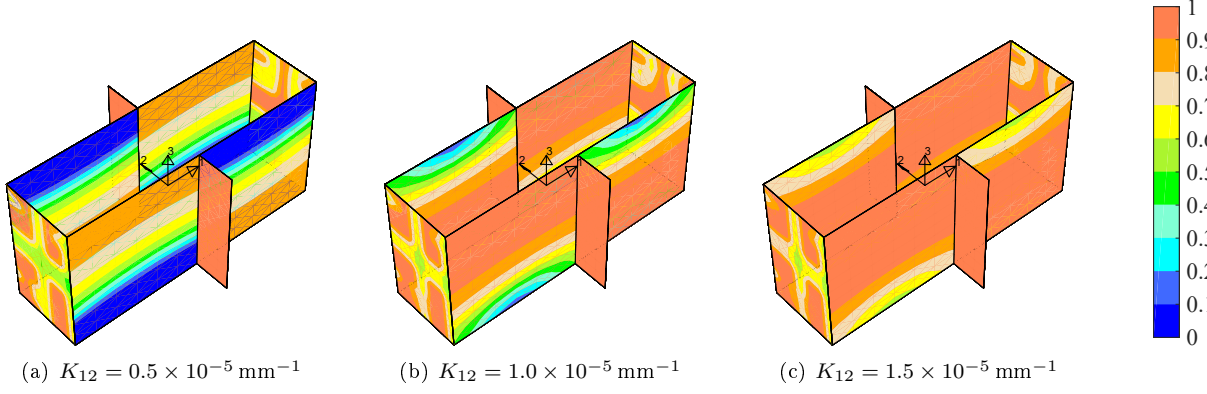
Figure 21: Distribution of damage variable D resulting at mortar joints obtained with micromechanical model for LH 6 and $\alpha_3 = t/4$.
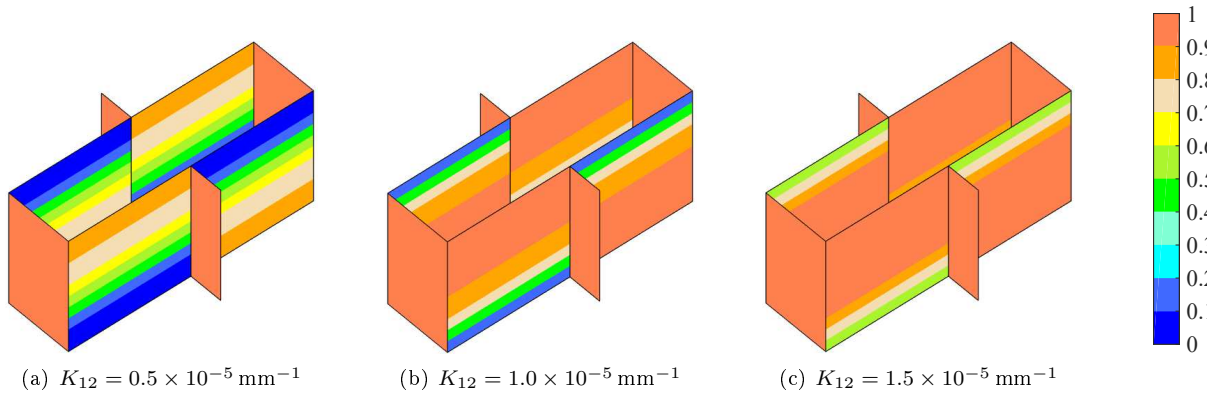

(a) $K_{12} = 0.5 \times 10^{-5}$ mm^{-1} (b) $K_{12} = 1.0 \times 10^{-5}$ mm^{-1} (c) $K_{12} = 1.5 \times 10^{-5}$ mm^{-1}

Figure 22: Distribution of damage variable D resulting at mortar joints obtained with TFA approach for LH 6, $\alpha_3 = t/4$ and $n_t = 10$.
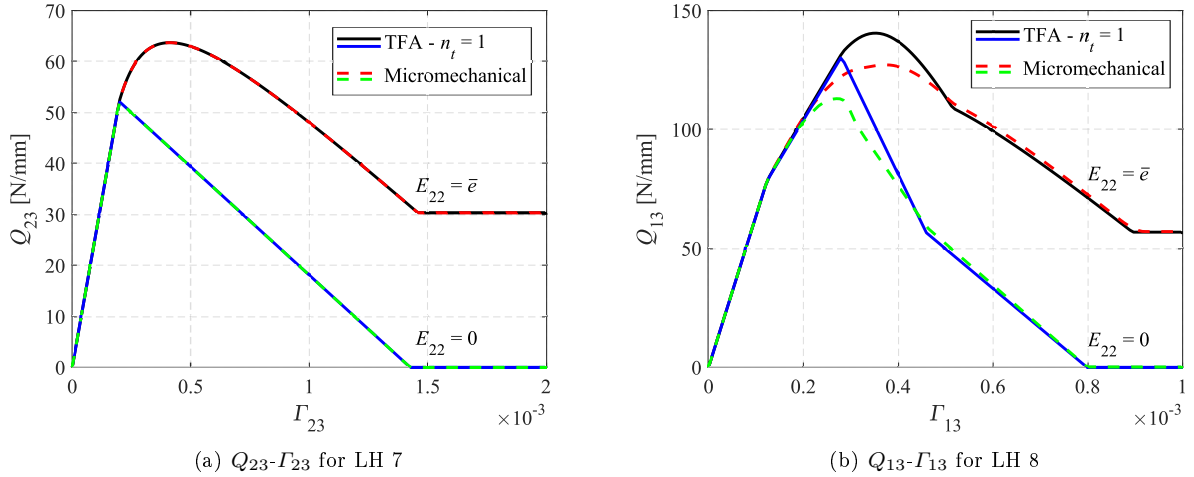

(a) Q_{23}-Γ_{23} for LH 7   (b) Q_{13}-Γ_{13} for LH 8

Figure 23: Average shear stresses Q_{23} and Q_{13} versus the average shear strains Γ_{23} and Γ_{13} for the UC subjected to LH 7 and 8, respectively, with influence of the tensile strain E_{22}.

the influence of sliding friction effects on the UC shear response. Only solutions obtained for $n_t = 1$ are considered for the TFA procedure, as very similar outcomes result by assuming $n_t > 1$. Indeed, when the UC is subjected to this strain state, almost uniform distribution of the nonlinear quantities results across thickness t and, thus, layer subdivision is not required.

Plots of the damage distributions resulting in the mortar joints for the micromechanical model are depicted

in Figure 24 and 26 for LH 7 and 8, respectively. Same distributions resulting for the TFA approach are depicted in Figure 25 and 27.
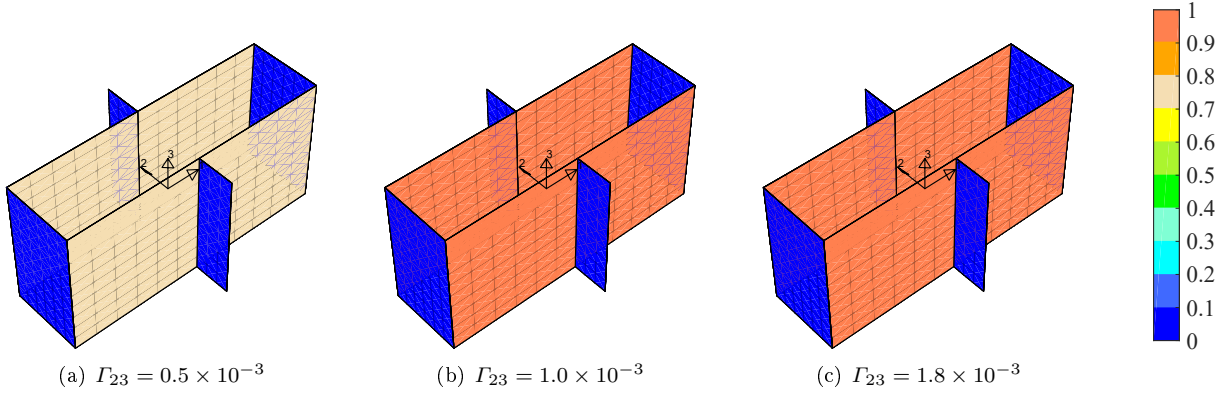

(a) $\Gamma_{23} = 0.5 \times 10^{-3}$ (b) $\Gamma_{23} = 1.0 \times 10^{-3}$ (c) $\Gamma_{23} = 1.8 \times 10^{-3}$

Figure 24: Distribution of damage variable D resulting at mortar joints obtained with micromechanical model for LH 7 and $E_{22} = \bar{e}$.

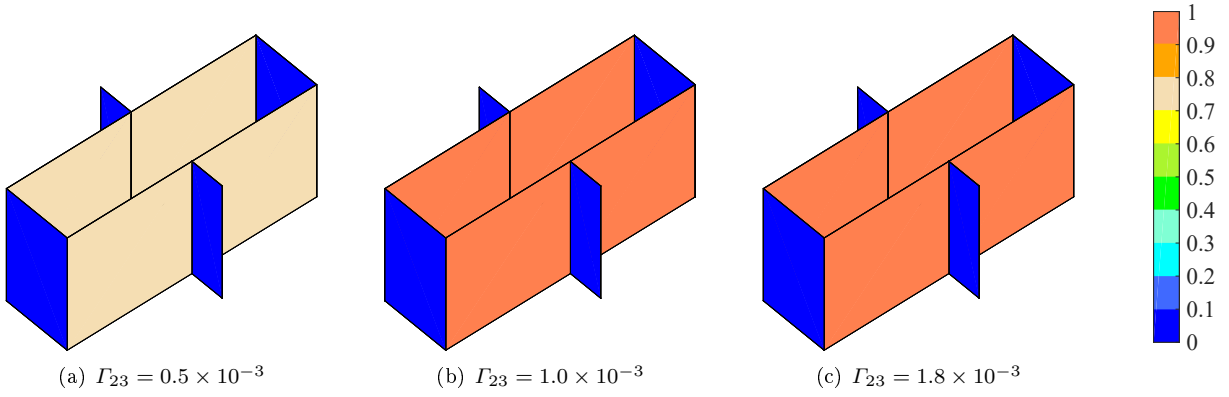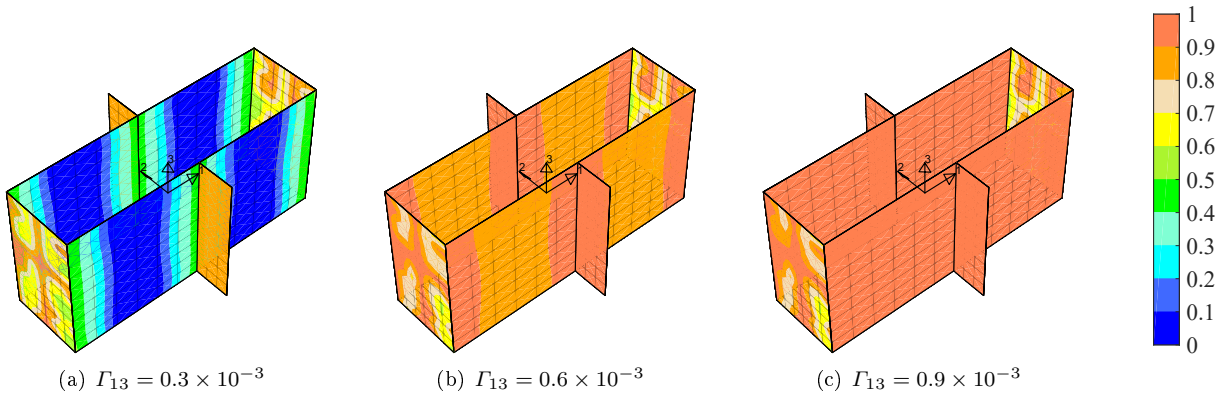(a) $\Gamma_{23} = 0.5 \times 10^{-3}$ (b) $\Gamma_{23} = 1.0 \times 10^{-3}$ (c) $\Gamma_{23} = 1.8 \times 10^{-3}$

Figure 25: Distribution of damage variable D resulting at mortar joints obtained with TFA approach for LH 7 and $E_{22} = \bar{e}$.

(a) $\Gamma_{13} = 0.3 \times 10^{-3}$ (b) $\Gamma_{13} = 0.6 \times 10^{-3}$ (c) $\Gamma_{13} = 0.9 \times 10^{-3}$

Figure 26: Distribution of damage variable D resulting at mortar joints obtained with micromechanical model for LH 8 and $E_{22} = \bar{e}$.

As shown, when shear strain in x_2-x_3 plane is applied (LH 7), TFA solution perfectly matches that obtained with the micromechanical model. Indeed, in this case, slip and damage only take place in bed mortar joints, with inelastic quantities showing uniform variations in the x_1 direction.

When shear strain in x_1-x_3 plane is applied (LH 8), a slight difference is noticed between the solutions obtained with the two models (Figure 23(b)). This occurs when slip in the mortar interfaces is small, i.e.
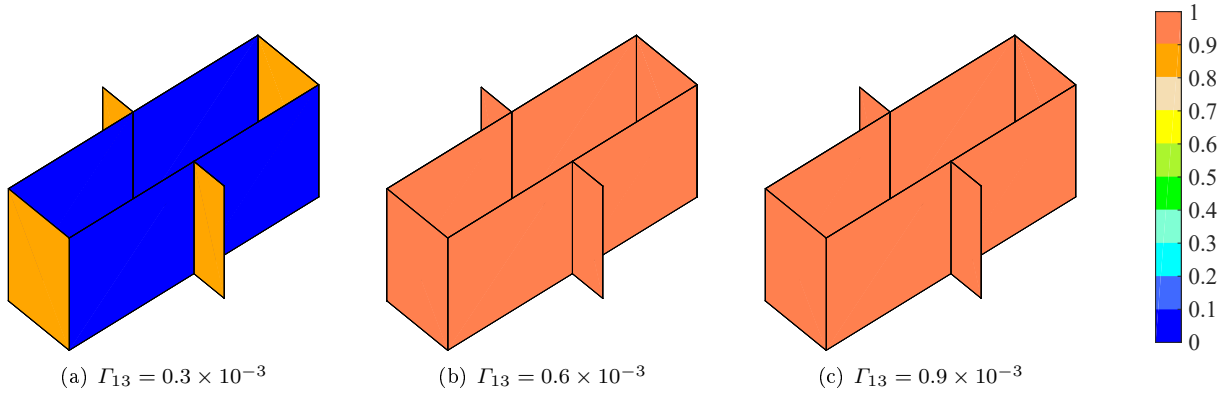
	1
	0.9
	0.8
	0.7
	0.6
	0.5
	0.4
	0.3
	0.2
	0.1
	0

(a) $\Gamma_{13} = 0.3 \times 10^{-3}$ (b) $\Gamma_{13} = 0.6 \times 10^{-3}$ (c) $\Gamma_{13} = 0.9 \times 10^{-3}$

Figure 27: Distribution of damage variable D resulting at mortar joints obtained with TFA approach for LH 8 and $E_{22} = \bar{e}$.

near the peak of the response curve, as nonuniform damage variations in the mortar joints are induced at this stage (Figure 26(a)). As already discussed, these nonuniform variations are not captured by the TFA procedure (Figure 27(a)). However, when slip in the mortar increases, damage tends to become uniform in the mortar (Figures 26 (b,c) and Figures 27 (b,c)) and good match results between micromechanical and TFA responses.

5.4. TFA vs micromechanical computational cost

In most of the analyzed cases, the proposed ROM permits to accurately describe the UC micromechanical response with significant computational saving.

The micromechanical model sketched in Figure 4 counts 6721 nodes and, consequently, the linearized system in Eq. (70) governing the global FE problem involves a high number of unknowns ($6721 \times 3 + 2 = 20165$). Moreover, to solve the nonlinear evolution problem of damage and friction, 3 history variables (HVs), i.e. damage (D) and the two slips (p_{T1}, p_{T2}), have to be stored at each quadrature point of the interface elements, resulting in a total number of HVs = 10080. Instead, when adopting the TFA technique, only 4 HVs (damage, slips, contact displacement jump) are required for each subset, with a total maximum number HVs = 120, obtained for the most accurate case (that is $n_t = 10$ and $n_s = 30$). These considerations justify the different computational effort required by the two modeling strategies. In Table 5 a comparison in terms of CPU time is provided for some of the benchmarks analyzed (LH 5 and LH 7). In cases of TFA computations, the indicated CPU time refers to that required by the iterative procedure reported in Table 2 to determine the macroscopic constitutive response. However, the proposed homogenization technique also requires to perform the two sets of preliminary elastic analyses to determine matrices $\overline{\mathbf{C}}$, $\overline{\mathbf{C}}_{\pi^i}$, $\overline{\mathbf{R}}^j$, $\overline{\mathbf{R}}^j_{\pi^i}$, resulting in additional CPU time equal to 142.47 s ($n_t = 1$), 184.27 s ($n_t = 2$) and 372.14 s ($n_t = 6$). It is worth remarking that these preliminary analyses have to be performed only once, before starting the multiscale analysis. Hence, computational saving is more and more relevant when the overall response of real structural elements or structures is studied, as same localization matrices are used for all the quadrature points of the mascroscopic mesh linked to UC with same geometric and mechanical properties. Moreover, such advantage emerges not only in comparison with the micromechanical strategy, but also with respect to the classical FE^2 multiscale approach, which requires to solve the UC micromechanical problem at each quadrature point of the macro model.

The influence of the layer subdivision across the UC thickness is shown in Table 5 for LH 5, considering $n_t = 2$ and $n_t = 6$.

All analyses were performed by means of the same personal computer under equal performance.

Table 5: Computational time required by the micromechanical and TFA approaches for some benchmarks.

LH	CPU time TFA $n_t = 1$	CPU time TFA $n_t = 2$	CPU time TFA $n_t = 6$	CPU time micromechanical
5 ($\alpha_2 = t$)		0.047 s	0.172 s	1029.20 s
7 ($E_{22} = \bar{e}$)	0.031 s			1733.32 s

6. Conclusions

The real texture of masonry walls can play a very important role in the mechanical response of structural elements. This point was very clear since old times; in fact, master builders knew well how to best arrange the bricks in masonry elements, like walls, dome and vaults. The texture leads to an anisotropic mechanical response of masonry and anisotropic failure conditions, that is a very relevant issue in many real structural cases.

Multiscale approach allows to perform structural analyses accounting for the real texture and microme- chanical behavior of the masonry material through homogenization of the representative volume element. The TFA is a reliable technique for performing homogenization of composites characterized by nonlinear response of the components.

In this paper, the TFA is developed in the framework of homogenization that considers two different models at two different scales: a structural shell model at the macroscale and a 3D Cauchy model at the microscale. The presence of two different models is important in order to reduce the computational burden at the macroscale and carefully account for the 3D micromechanical mechanisms at the lower scale.

Even in this case, the TFA procedure, whose limits mainly rely on the pre-definition of the regions where nonlinear effects can occur and the pre-assumed variation of these latter, demonstrated very good perfor- mances. Summarizing, it has been seen that:

- for loading histories involving membrane strains, the TFA allows to obtain results in very good accor- dance with the FE micromechanical analyses, even considering only one subdivision in subsets along the thickness coordinate;

- for loading histories involving out-of-plane shear strains, an analogous result is obtained, so that it is sufficient only one subdivision in the masonry wall thickness to get very satisfactory results;

- for bending problem around the x_1 axis, it is demonstrated that increasing the number of subsets in the thickness convergence to the FE solution is reached. In fact, very accuracy results (with respect to the FE reference solution) are recovered setting $n_t = 10$;

- less accurate, but globally satisfactory, results are obtained for bending around the x_2 axis and torsional loading condition; this is due to the nonuniform inelastic jumps arising in the subsets of the TFA model, in contrast to one of the main assumption of the developed technique.

Finally, it could be concluded that:

- the use of different schemes at the two scales presents an indubitable computational advantage in studying the nonlinear response of periodic masonry walls;

- the TFA procedure reveals to be, even in this application, a very reliable and effective procedure for resorting to a reduced order model.

Inaccuracies of the proposed TFA procedure are probably negligible when it is implemented in a full scale model and used to analyze a whole structure. This point will be investigated in future researches. It is worth

pointing out that, as a consequence of the degrading constitutive law derived for the structural macroscopic point by means of the TFA procedure applied to the masonry UC, localization phenomena are likely to occur at the macroscale. Thus, to avoid pathological mesh-dependency of the FE numerical solution a regularization technique needs to be adopted. Various approaches could be selected to this purpose, as for example a nonlocal integral macroscopic model could be formulated introducing the nonlocal definition of the shell strain measures [11], as well as enriched (Cosserat), fracture mechanics, smeared crack models could be adopted. In this paper, even if the macromechanical problem is not explicitly treated, it is implicitly assumed that a smeared crack approach is used at the macroscale. Thus, a relation between the energy dissipation and the size of the UC, with the damage energy and the localization width should be introduced.

Further improvements of the proposed model could be performed considering nonuniform inelastic jumps or adopting specific mathematical procedures, as that proposed in [7], to get an optimal distribution of subsets in the UC. Moreover, further nonlinear mechanisms could be introduced in the TFA procedure as those involving the bricks, as well other masonry textures could be easily studied by properly setting location and number of the nonlinear subsets.

Nonlinear geometric effects, neglected in the above proposed procedure, could also be taken into account. These could be particularly relevant for some typical masonry structural elements, like slender columns, walls and arches where stability issues need to be tackled [2]. An effective and promising methodolody to include nonlinear geometry behavior is the corotational approach, already employed in [2], that would permit to account for large displacements at the macroscale level without modifying the microscopic formulation, that is the TFA technique.

Eventually, the developed TFA-based homogenization procedure will be introduced in a multiscale framework and used to study real-scale structural problems.

Acknowledgements

References

[1] D. Addessi, M.L. De Bellis, and E. Sacco. A micromechanical approach for the Cosserat modeling of composites. *Meccanica*, 51:194–214, 2016.

[2] D. Addessi, P. Di Re, and E. Sacco. Micromechanical and multiscale computational modeling for stability analysis of masonry elements. *Engineering Structures*, 211:110428, 2020.

[3] D. Addessi, C. Gatta, S. Marfia, and E. Sacco. Multiscale analysis of in-plane masonry accounting for degradation and frictional effects. *Journal for Multiscale Computational Engineering*, 2020.

[4] D. Addessi and E. Sacco. Enriched plane state formulation for nonlinear homogenization of in-plane masonry wall. *Meccanica*, 51(11):2891–2907, 2016.

[5] D. Addessi and E. Sacco. Nonlinear analysis of masonry panels using a kinematic enriched plane state formulation. *International Journal of Solids and Structures*, 90:194–214, 2016.

[6] D. Addessi and E. Sacco. Homogenization of heterogeneous masonry beams. *Meccanica*, 53(7):1699–1717, 2018.

[7] G. Alaimo, F. Auricchio, S. Marfia, and E. Sacco. Optimization clustering technique for PieceWise Uniform Transformation Field Analysis homogenization of viscoplastic composites. *Computational Mechanics*, 2019.

[8] A. Anthoine. Derivation of the in-plane elastic characteristics of masonry through homogenization theory. *International Journal of Solids and Structures*, 32(2):137–163, 1995.

[9] A. Anthoine. Homogenization of periodic masonry: plane stress, generalized plane strain or 3D modelling? *Communications in Numerical Methods in Engineering*, 13:319–326, 1997.

[10] A. Bacigalupo and L. Gambarotta. Second-order computational homogenization of heterogeneous materials with periodic microstructure. *ZAMM: Journal of Applied Mathematics and Mechanics*, 90(11):796–811, 2011.

[11] Z. P. Bazant and M. Jirasek. Nonlocal integral formulations of plasticity and damage: survey of progress. *Journal of Engineering Mechanics ASCE*, 128(11):1119–1149, 2002.

[12] A. Cecchi and K. Sab. A homogenized Reissner–Mindlin model for orthotropic periodic plates: Application to brickwork panels. *International Journal of Solids and Structures*, 44(18):6055–6079, 2007.

[13] A. Cecchi and K. Sab. A homogenized Love-Kirchhoff model for out-of-plane loaded random 2D lattices: Application to "quasi-periodic" brickwork panels. *International Journal of Solids and Structures*, 46:2907–2919, 2009.

[14] A. M. D'Altri, S. de Miranda, S. Castellazzi, and Sarhosis V. A 3D detailed micro-model for the in-plane and out-of-plane numerical analysis of masonry panels. *Computers & Structures*, 206:18–30, 2018.

[15] A. M. D'Altri, V. Sarhosis, G. Milani, J Rots, S. Cattari, S. Lagomarsino, E. Sacco, A. Tralli, G. Castellazzi, and S. de Miranda. Modeling strategies for the computational analysis of unreinforced masonry structures: Review and classification. *Archives of Computational Methods in Engineering*, 26:1–33, 2019.

[16] M.L. De Bellis and D. Addessi. A Cosserat based multi-scale model for masonry structures. *International Journal for Multiscale Computational Engineering*, 9(5):543–563, 2011.

[17] G.J. Dvorak. Transformation field analysis of inelastic composite materials. *Proceedings of the Royal Society of London A*, 437:311–327, 1992.

[18] F. Fritzen and T. Bohlke. Three-dimensional finite element implementation of the nonuniform transformation field analysis. *International Journal for Numerical Methods in Engineering*, 278:186–217, 2014.

[19] G. Giambanco, S. Rizzo, and R. Spallino. Numerical analysis of masonry structures via interface models. *Computer Methods in Applied Mechanics and Engineering*, 190:6493–6511, 2001.

[20] F. Lebon. *Modeling the interfaces in masonry structures*, pages 213–240. Springer Vienna, Vienna, 2014.

[21] L. Macorini and B. A. Izzuddin. A non-linear interface element for 3D mesoscale analysis of brick-masonry structures. *International Journal for Numerical Methods in Engineering*, 85(12):1584–1608, 2011.

[22] T. J. Massart, R. H. J. Peerlings, and M. G. D. Geers. An enhanced multi-scale approach for masonry wall computations with localization of damage. *International Journal for Numerical Methods in Engineering*, 69(5):1022–1059, 2007.

[23] T. J. Massart, R. H. J. Peerlings, and M. G. D. Geers. Structural damage analysis of masonry walls using computational homogenization. *International Journal of Damage Mechanics*, 16:199–226, 2007.

[24] B.C.N. Mercatoris, Ph. Bouillard, and T.J. Massart. Multi-scale detection of failure in planar masonry thin shells using computational homogenisation. *Engineering Fracture Mechanics*, 76(4):479–499, 2009.

[25] B.C.N. Mercatoris and T.J. Massart. A coupled two-scale computational scheme for the failure of periodic quasi-brittle thin planar shells and its application to masonry. *International Journal for Numerical Methods in Engineering*, 85:1177–1206, 2011.

[26] J.C. Michel and P. Suquet. Nonuniform transformation field analysis. *International Journal for Solids and Structures*, 40:6937–6955, 2003.

[27] E. Minga, L. Macorini, and B. A. Izzuddin. A 3D mesoscale damage-plasticity approach for masonry structures under cyclic loading. *Meccanica*, 53(7):1591–1611, 2018.

[28] M. Petracca, L. Pelà, R. Rossi, S. Oller, G. Camata, and E. Spacone. Multiscale computational first order homogenization of thick shells for the analysis of out-of-plane loaded masonry walls. *Computer Methods in Applied Mechanics and Engineering*, 315:273–301, 2017.

[29] V. Sepe, S. Marfia, and E. Sacco. A nonuniform TFA homogenization technique based on piecewise interpolation functions of the inelastic field. *International Journal of Solids and Structures*, 50(5):725 − 742, 2013.

[30] L. Snozzi and J.-F. Molinari. A cohesive element model for mixed mode loading with frictional contact capability. *International Journal for Numerical Methods in Engineering*, 93(5):510–526, 2013.

[31] C. V. Verhoosel, J. J. C. Remmers, M. A. Gutiérrez, and R. de Borst. Computational homogenization for adhesive and cohesive failure in quasi-brittle solids. *International Journal for Numerical Methods in Engineering*, 83(8-9):1155–1179, 2010.

[32] O. C. Zienkiewicz, R. L. Taylor, and J. Z. Zhu. *The finite element method: its basis and fundamentals*. Elsevier, 2005.